Article

Cell

Temporal Control of Mammalian Cortical Neurogenesis by m^{6}A Methylation

Graphical Abstract

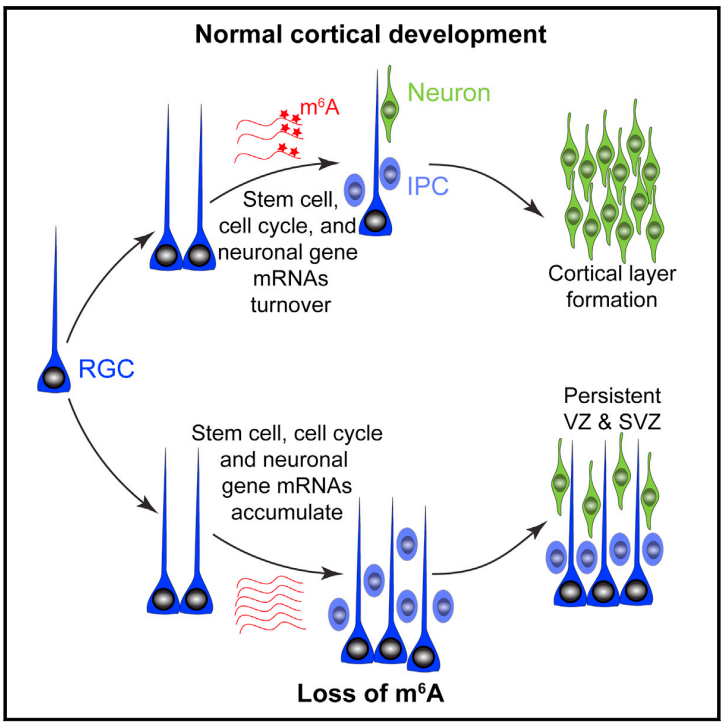

Highlights

- m^{6}A depletion leads to prolonged cell-cycle progression of cortical neural progenitors
- m^{6}A promotes decay of tagged neurogenesis-related transcripts
- Transcriptional prepatterning for normal cortical neurogenesis
- Conserved and unique m^{6}A landscapes in mouse and human cortical neurogenesis

Authors

Ki-Jun Yoon, Francisca Rojas Ringeling, Caroline Vissers, ..., Chuan He, Guo-li Ming, Hongjun Song

Correspondence

gming@pennmedicine.upenn.edu (G.-l.M.), shongjun@pennmedicine.upenn.edu (H.S.)

In Brief

m^{6}A-dependent mRNA decay is critical for proper transcriptional prepatterning in mammalian cortical neurogenesis.

Yoon et al., 2017, Cell *171*, 877–889
November 2, 2017
http://dx.doi.org/10.1016/j.cell.2017.09.003

CellPress

Article

Cell

Temporal Control of Mammalian Cortical Neurogenesis by m^{6}A Methylation

Ki-Jun Yoon,[1,2,3,15] Francisca Rojas Ringeling,[4,15] Caroline Vissers,[5,15] Fadi Jacob,[6] Michael Pokrass,[5] Dennisse Jimenez-Cyrus,[8] Yijing Su,[1] Nam-Shik Kim,[1,2] Yunhua Zhu,[2] Lily Zheng,[4] Sunghan Kim,[2] Xinyuan Wang,[1] Louis C. Doré,[9] Peng Jin,[10] Sergi Regot,[7] Xiaoxi Zhuang,[11] Stefan Canzar,[12] Chuan He,[9] Guo-li Ming,[1,2,3,5,6,8,13,*] and Hongjun Song[1,2,3,4,5,6,8,13,14,16,*]

[1]Department of Neuroscience and Mahoney Institute for Neurosciences, University of Pennsylvania, Philadelphia, PA 19104, USA
[2]Institute for Cell Engineering
[3]Department of Neurology
[4]The Pre-doctoral Human Genetic Training Program
[5]The Biochemistry, Cellular, and Molecular Biology Graduate Program
[6]The Solomon H. Snyder Department of Neuroscience
[7]Department of Molecular Biology and Genetics
[8]The Cellular and Molecular Medicine Graduate Program
Johns Hopkins University School of Medicine, Baltimore, MD 21205, USA
[9]Departments of Chemistry and Biochemistry and Molecular Biology, Institute for Biophysical Dynamics, Howard Hughes Medical Institute, University of Chicago, Chicago, IL 60637, USA
[10]Department of Human Genetics, School of Medicine, Emory University, Atlanta, GA 30322, USA
[11]Department of Neurobiology, University of Chicago, Chicago, IL 60637, USA
[12]Gene Center, Ludwig-Maximilians-Universität München, 81377 Munich, Germany
[13]The Institute for Regenerative Medicine
[14]The Epigenetics Institute, Perelman School for Medicine
University of Pennsylvania, Philadelphia, PA 19104, USA
[15]These authors contributed equally
[16]Lead Contact
*Correspondence: gming@pennmedicine.upenn.edu (G.-l.M.), shongjun@pennmedicine.upenn.edu (H.S.)
http://dx.doi.org/10.1016/j.cell.2017.09.003

SUMMARY

N^6-methyladenosine (m^{6}A), installed by the Mettl3/Mettl14 methyltransferase complex, is the most prevalent internal mRNA modification. Whether m^{6}A regulates mammalian brain development is unknown. Here, we show that m^{6}A depletion by *Mettl14* knockout in embryonic mouse brains prolongs the cell cycle of radial glia cells and extends cortical neurogenesis into postnatal stages. m^{6}A depletion by *Mettl3* knockdown also leads to a prolonged cell cycle and maintenance of radial glia cells. m^{6}A sequencing of embryonic mouse cortex reveals enrichment of mRNAs related to transcription factors, neurogenesis, the cell cycle, and neuronal differentiation, and m^{6}A tagging promotes their decay. Further analysis uncovers previously unappreciated transcriptional prepatterning in cortical neural stem cells. m^{6}A signaling also regulates human cortical neurogenesis in forebrain organoids. Comparison of m^{6}A-mRNA landscapes between mouse and human cortical neurogenesis reveals enrichment of human-specific m^{6}A tagging of transcripts related to brain-disorder risk genes. Our study identifies an epitranscriptomic mechanism in heightened transcriptional coordination during mammalian cortical neurogenesis.

INTRODUCTION

Proper development of the nervous system is critical for its function, and deficits in neural development have been implicated in many brain disorders, such as microcephaly, autistic spectrum disorders, and schizophrenia (Jamuar and Walsh, 2015; Taverna et al., 2014). In the embryonic mouse cortex, radial glia cells (RGCs) function as neural stem cells, sequentially giving rise to neurons residing in different cortical layers and then switching to glial production before their depletion during early postnatal stages (Taverna et al., 2014). Such a precise and predictable developmental schedule requires a highly coordinated genetic program (Okano and Temple, 2009). Indeed, previous studies have revealed transcriptional cascades that orchestrate the dynamics of mammalian cortical neurogenesis (Martynoga et al., 2012; Miller et al., 2014; Nord et al., 2015). Recent discoveries of widespread mRNA chemical modifications (Zhao et al., 2017a) raise the question of whether this mechanism plays any regulatory role in cortical neurogenesis.

Modified nucleotides in mRNAs were initially discovered over 40 years ago, but little was known about the extent, transcript identities, and potential functions of various reversible chemical modifications until very recently (Zhao et al., 2017a). High-throughput sequencing approaches have revealed a dynamic "epitranscriptome" landscape for many mRNA modifications in various organisms, including N^6-methyladenosine (m^{6}A), N^1-methyladenosine (m^{1}A), 5-methylcytosine (m^{5}C), 5-hydroxymethylcytosine (hm^{5}C), and pseudouridine (ψ) (Li et al., 2016).

Among these modifications, m^{6}A is the most abundant internal modification in mRNAs of eukaryotic cells (Desrosiers et al., 1975). m^{6}A profiling with cell lines has revealed m^{6}A sites in over 25% of human transcripts, with enrichment in long exons, and near transcription start sites and stop codons (Meyer and Jaffrey, 2014). In mammals, m^{6}A is installed by the methyltransferase complex, which consists of Mettl3 (methyltransferase-like 3), Mettl14, Wtap (Wilms tumor 1-associated protein), KIAA1429, RBM15 (RNA-binding motif protein 15), and its paralog (RBM15B) (Patil et al., 2016), whereas its removal is mediated by the demethylases Fto (fat mass and obesity-associated) and Alkbh5 (alkB homolog 5) (Zhao et al., 2017a). Recent in vitro studies have identified multiple functions of m^{6}A in mRNA metabolism, from processing in the nucleus to translation and decay in the cytoplasm (Zhao et al., 2017a). The field has just started to investigate physiological functions of m^{6}A. For example, *Mettl3* or *Mettl14* knockdown reduces m^{6}A levels and decreases self-renewal of primed mouse embryonic stem cells (mESCs) (Wang et al., 2014a), whereas *Mettl3* knockout naive mESCs exhibit improved self-renewal and impaired differentiation due to dysregulated decay of m^{6}A-tagged transcripts, such as *Nanog* (Batista et al., 2014; Geula et al., 2015).

Identification of the molecular machinery mediating m^{6}A mRNA methylation provides an entry point to explore physiological functions of this pathway in vivo. Studies of *Drosophila* development showed that m^{6}A methylation regulates sex determination and neuronal functions by modulating mRNA splicing (Haussmann et al., 2016; Lence et al., 2016). In zebrafish embryos, m^{6}A-tagging promotes clearance of maternal mRNAs and maternal-to-zygotic transition (Zhao et al., 2017e). In mice, germline *Mettl3* deletion results in early embryonic lethality (Geula et al., 2015). Nothing is known about the role of m^{6}A signaling during mammalian embryonic brain development in vivo. Here, we used the *Mettl14* conditional knockout (cKO) mouse as a model to examine m^{6}A function in embryonic cortical neurogenesis in vivo. We further investigated underlying cellular and molecular mechanisms. Finally, we extended our analysis to human embryonic cortical neurogenesis using induced pluripotent stem cell (iPSC)-derived forebrain organoids and compared m^{6}A-mRNA landscapes between mouse and human cortical neurogenesis. Together, our results reveal critical epitranscriptomic control of mammalian cortical neurogenesis and provide insight into mechanisms underlying this highly coordinated developmental program.

RESULTS

Nervous System *Mettl14* Deletion Extends Cortical Neurogenesis into Postnatal Stages

We first investigated the expression pattern of molecular players mediating m^{6}A signaling during mouse embryonic cortical neurogenesis. Mining the recently published single-cell RNA-sequencing (RNA-seq) dataset of RGCs and their progeny (Telley et al., 2016) revealed the highest *Mettl14* expression in RGCs and relatively constant levels of m^{6}A methyltransferase components (*Mettl3* and *Wtap*), demethylases (*Fto* and *Alkbh5*), and m^{6}A readers (*Ythdf2* and *Ythdf3*) during neurogenesis (Figure S1A). We next conditionally deleted *Mettl14* in the developing mouse nervous system starting at embryonic day 11.5 (E11.5) using the *Nestin-Cre;Mettl14$^{f/f}$* cKO model (Figure S1B). We confirmed *Mettl14* deletion at the protein level with western blot analysis of E17.5 brains (Figure S1B). The cKO animals were smaller by postnatal day 5 (P5) than wild-type (WT) littermates, and all cKO animals died before P25 (Figures S1C and S1D). Thus, the function of m^{6}A molecular machinery in the nervous system is indispensable for life in the mammalian system.

We then examined cortical structures at P5. cKO mice exhibited enlarged ventricles with an adjacent dense layer of cells that resembled the embryonic germinal zone (Figure 1A). Immunohistological analysis showed the presence of Pax6$^+$ and Nestin$^+$ cells with radial fibers along the ventricle in cKO mice, but not in WT mice (Figures 1A and 1B). During mouse cortical development, Pax6$^+$ RGCs are largely depleted by P5 (Dwyer et al., 2016). In contrast, a substantial number of Pax6$^+$ cells were present in cKO mice at P5 (Figure 1C). Neurogenic Pax6$^+$ RGCs give rise to intermediate progenitor cells (IPCs) expressing Tbr2/Eomes (Englund et al., 2005). The presence of Pax6$^+$ cells in cKO mice was accompanied by Tbr2$^+$ IPCs, which were absent in WT mice by P5 (Figures 1D and 1E). To confirm that cortical neurogenesis continued postnatally, we pulsed animals with ethynyldeoxyuridine (EdU) at P5 and analyzed 2 days later. Significant numbers of EdU$^+$Pax6$^+$ proliferating RGCs, EdU$^+$Tbr2$^+$ IPCs, and EdU$^+$Tbr2$^+$TuJ1$^+$ neuroblasts were present in cKO mice, but very few were present in WT littermates (Figures 1F and 1G). These results indicate that cKO mice maintain neurogenic RGCs with extended cortical neurogenesis into postnatal stages.

To further characterize the impact of *Mettl14* deletion on cortical development, we examined neuronal subtype and glia production. We pulsed animals with EdU at E15.5 and examined them at P5. Compared to WT littermates, cKO mice exhibited a significantly decreased number of EdU$^+$Satb2$^+$ neurons, suggesting a deficit in producing late-born upper-layer neurons (Figures 1H and 1I). Direct measurement of the number of different cortical neuron subtypes also showed a reduced number of Satb2$^+$ upper-layer neurons but comparable numbers of Tbr1$^+$ and Ctip2/Bcl11b$^+$ lower-layer early-born neurons in P5 cKO mice (Figures S1E and S1F). On the other hand, Ctip2$^+$ neurons were reduced in number in the E17.5 cKO cortex, suggesting a delay in the production of neuron subtypes of different cortical layers rather than differentiation deficits (Figures S1G and S1H). In addition, we observed a significant decrease in the number of s100β$^+$ astrocytes in cKO mice at P5 (Figures 1J and 1K). Together, these results indicate that Mettl14 function is critical for proper temporal progression of neurogenesis and gliogenesis during mouse cortical development in vivo.

Mettl14 Deletion in Neural Progenitor Cells Leads to Protracted Cell-Cycle Progression

Given the well-defined temporal progression of cortical neurogenesis from RGCs (Okano and Temple, 2009), we suspected that there could be RGC deficits during embryonic stages in cKO mice. Interkinetic nuclear migration (INM), the periodic movement of the cell nucleus in phase with cell-cycle progression, is a common feature of developing neuroepithelial (Taverna

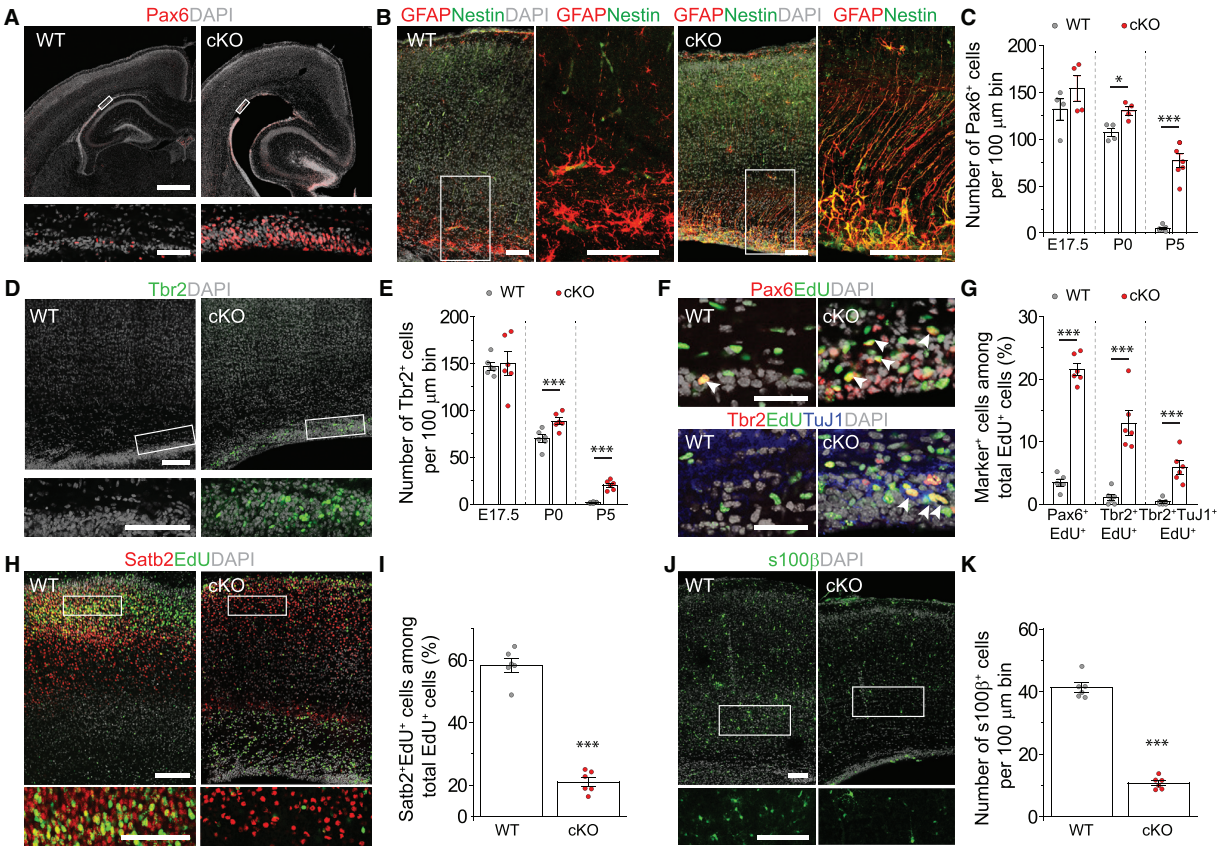

Figure 1. Nervous System *Mettl14* Deletion Results in Residual Radial Glia Cells and Ongoing Neurogenesis in the Postnatal Mouse Cortex

(A–C) Presence of neurogenic RGCs in P5 *Nestin-Cre;Mettl14*$^{f/f}$ cKO cortices. Shown are sample confocal images (A and B) and quantification (C). Regions in white boxes are shown at a higher magnification. Scale bars represent 500 μm (A, top), 50 μm (A, bottom), and 100 μm (B). Values in (C) represent mean ± SEM (n = 4–7; ***p < 0.001; *p < 0.05; unpaired Student's t test).

(D and E) Presence of IPCs in P5 cKO cortices. Shown are sample confocal images (D; scale bars, 100 μm) and quantification (E). Values represent mean ± SEM (n = 6; ***p < 0.001; **p < 0.01; unpaired Student's t test).

(F and G) Ongoing neurogenesis in P5 cKO cortices. P5 pups were injected with EdU and analyzed 48 hr later. Sample confocal images of the ventricular side of the primary somatosensory cortex are shown in (F). Arrows indicate Pax6$^+$EdU$^+$ cells (top) and Tbr2$^+$TuJ1$^+$EdU$^+$ cells (bottom). Scale bars represent 100 μm. Quantification of EdU$^+$ cells with different markers is shown in (G). Values represent mean ± SEM (n = 6; ***p < 0.001; unpaired Student's t test).

(H–K) Reduced production of upper-layer neurons and astrocytes in cKO cortices. Pregnant mice were injected with EdU at E15.5 and analyzed at P5. Shown are sample confocal images (H and J; scale bars, 100 μm) and quantification (I and K). Values represent mean ± SEM (n = 6; ***p < 0.001; unpaired Student's t test). See also Figure S1.

et al., 2014). We pulsed animals with EdU at E17.5 to label cells in S phase and followed positions of nuclei in EdU$^+$Pax6$^+$ RGCs (Figure 2A). While there was no difference at 0.5 hr after EdU labeling, nuclei of labeled RGCs were positioned further away from the ventricular surface at 6 hr in cKO mice than in WT mice (Figure 2B), suggesting delayed INM and potential cell-cycle deficits. To directly examine the S to M phase transition of the cell cycle, we analyzed expression of phospho-histone 3 (pH3), an M phase marker, 2 hr after EdU labeling (Figure 2C). We found a significant decrease in the percentage of EdU$^+$pH3$^+$Pax6$^+$ cells among all pH3$^+$Pax6$^+$ cells in cKO mice, suggesting a prolonged S to M phase transition of RGCs (Figure 2D). To examine the cell-cycle exit of proliferating neural progenitors, we analyzed expression of Ki67 (a proliferation marker) 24 hr after EdU labeling (Figure 2E). We found a significant decrease in the percentage of Ki67-negative cells among EdU$^+$ cells in cKO mice, indicating a delay in cell-cycle exit (Figure 2F).

To address the cell-intrinsic effect of *Mettl14* deletion on cell-cycle progression, we performed time-lapse imaging of individual cortical neural progenitor cells (NPCs) cultured from E13.5 mouse cortex. We used a dual-reporter system with nuclear localized H2B-mCherry and a GFP-tagged Cdk2 substrate, DNA helicase B (DHB) (Spencer et al., 2013). Cdk2 becomes active during the G_1 to S transition and phosphorylates DHB-GFP, which is then translocated from the nucleus to the cytoplasm. Therefore, the presence of GFP in the mCherry$^+$ nucleus indicates cells in G_1 phase, whereas translocation to the cytoplasm indicates S phase initiation, and continual buildup of

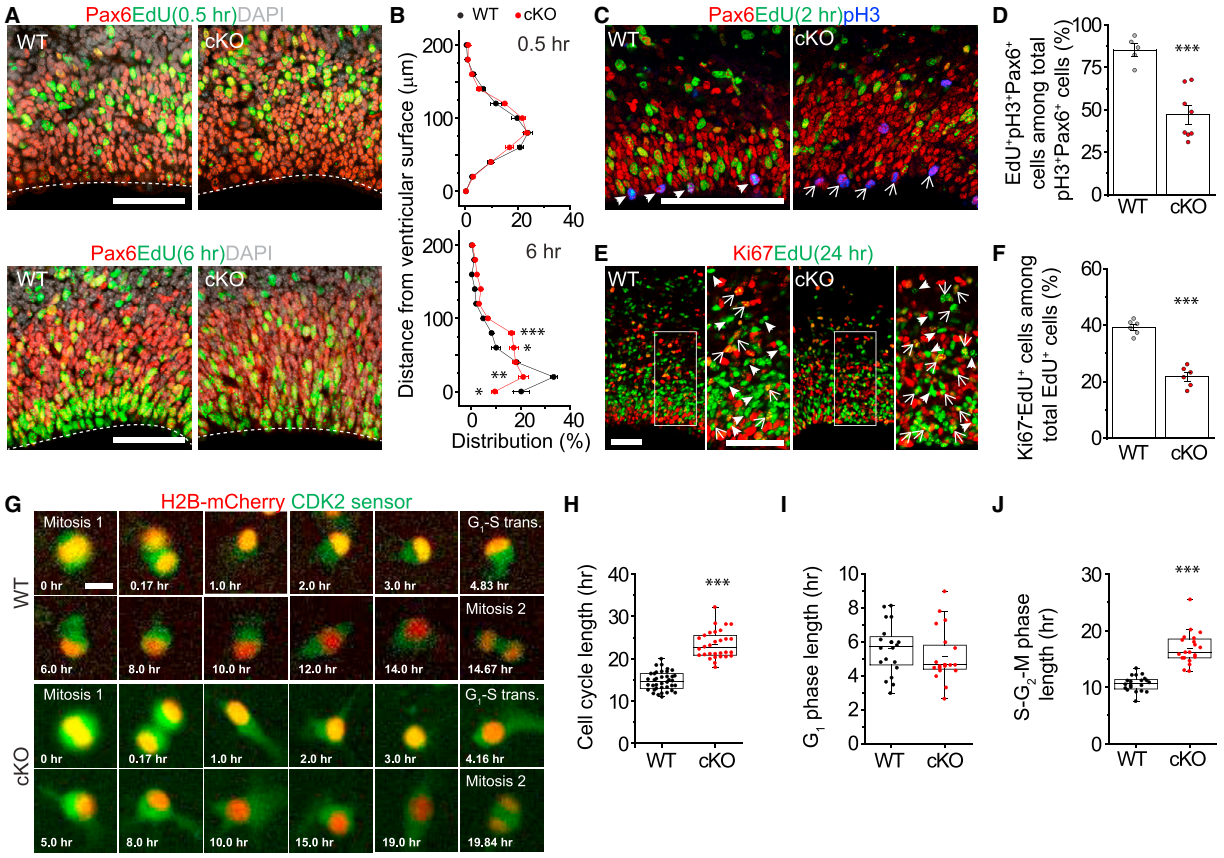

Figure 2. *Mettl14*$^{-/-}$ RGCs and NPCs Exhibit Prolonged Cell-Cycle Progression

(A and B) Abnormal INM of RGCs in *Mettl14* cKO cortices. Pregnant mice were injected with EdU at E17.5 and analyzed 0.5 or 6 hr later. Shown are sample confocal images (A; scale bars, 50 μm) and quantification of the distance from Pax6$^+$EdU$^+$ nuclei to the ventricular surface (B). Values for the percentages of nuclei in each 20-μm bin represent mean ± SEM (n = 4; ***p < 0.001; **p < 0.01; *p < 0.05; unpaired Student's t test).

(C and D) Delayed S to M phase transition of RGCs in *Mettl14* cKO mice. Pregnant mice were injected with EdU at E17.5 and analyzed 2 hr later. Shown in (C) are sample confocal images. Arrowheads point to Pax6$^+$pH3$^+$EdU$^+$ cells, and arrows point to Pax6$^+$pH3$^+$EdU$^-$ cells. Scale bar, 50 μm. Shown in (D) is the quantification of the percentage of Pax6$^+$pH3$^+$EdU$^+$ cells, representing cells proceeded from S to M phase during the 2-hr chase, among total Pax6$^+$pH3$^+$ cells. Values represent mean ± SEM (n = 5 for WT and n = 8 for cKO; ***p < 0.001; unpaired Student's t test).

(E and F) Delayed cell-cycle exit of neural progenitors in *Mettl14* cKO mice. Pregnant mice were injected with EdU at E17.5 and analyzed 24 hr later. Shown in (E) are sample confocal images. Arrowheads point to Ki67$^-$EdU$^+$ cells, and arrows point to Ki67$^+$EdU$^-$ cells. Scale bar, 50 μm. Shown in (F) is the quantification of the percentage of Ki67$^-$EdU$^+$ cells, representing cells exited from cell cycle, among total EdU$^+$ cells. Values represent mean ± SEM (n = 6; ***p < 0.001; unpaired Student's t test).

(G–J) Time-lapse imaging analysis of mouse NPCs showing prolonged S-G_2-M phase length in the absence of *Mettl14*. WT and cKO mouse NPCs were electroporated with plasmid co-expressing a Cdk2 sensor (green) and the H2B-mCherry nuclear marker (red), cultured for 2 days, and imaged for 48 hr. Shown in (G) are sample time-lapse images with time stamps. Scale bars, 10 μm. Also shown are boxplots of quantifications for the total cell-cycle length (H; n = 38 for WT and n = 30 for cKO), G_1 phase length (I; n = 20), and S-G_2-M phase length (J; n = 20). Each dot represents data from one NPC (***p < 0.001; unpaired Student's t test). See also Figure S2.

cytoplasmic GFP occurs until mitosis (Figure S2A). Quantification of the length between sequential mitoses showed an increase of the total cell-cycle length in *Mettl14* cKO NPCs (Figures 2G and 2H; Movies S1 and S2). Further analysis of different cell-cycle phases revealed a specific increase of the S-G_2-M phases in the absence of *Mettl14* but no difference in the G_1 phase (Figures 2I and 2J).

To quantify cell-cycle characteristics at the population level, we pulsed NPCs with EdU for 30 min and performed flow cytometry analysis 0 or 5 hr later (Figure S2B). We found a significant decrease in the percentage of EdU$^+$ cells that divided in *Mettl14* cKO NPCs compared to WT at 5 hr, confirming a delay in cell-cycle progression (Figures S2C and S2D).

Mettl3 Regulates Embryonic Cortical Neurogenesis

Consistent with the finding that Mettl14 is a critical component of the m^{6}A methyltransferase complex (Wang et al., 2017), *Mettl14* deletion led to a significant reduction of m^{6}A levels in mRNAs

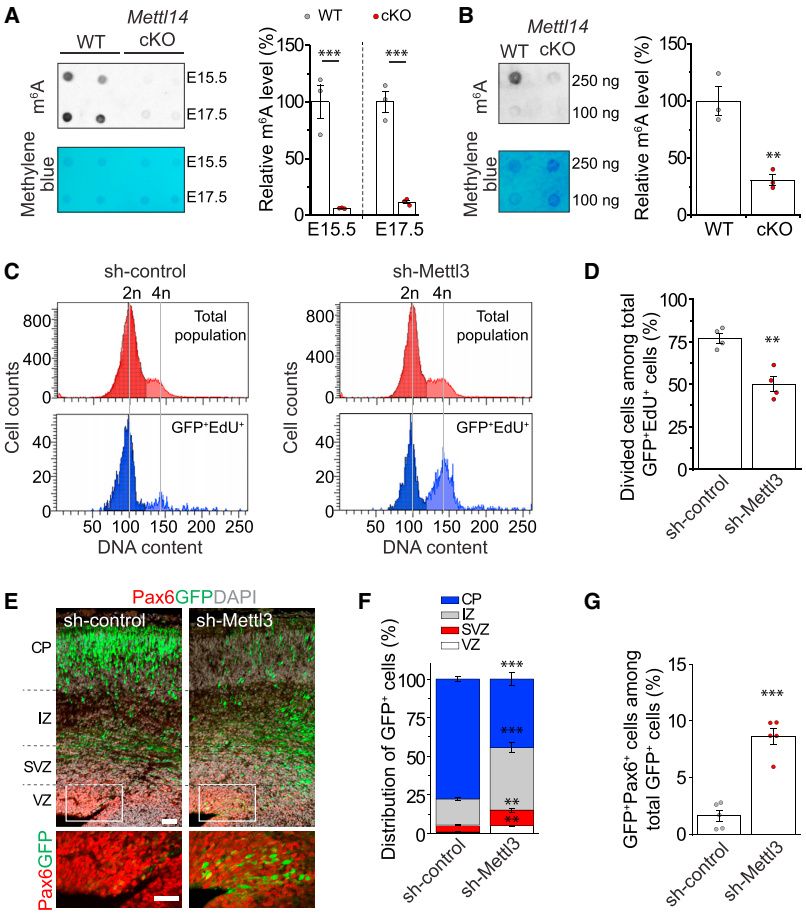

Figure 3. Mettl3 Regulates Cell-Cycle Progression of NPCs and Maintenance of Embryonic Cortical RGCs

(A) Depletion of m^{6}A tagging on mRNAs purified from E15.5 and E17.5 *Mettl14* cKO mouse forebrain. Shown in the left panels are sample images of m^{6}A dot blot and methylene blue staining (for loading controls). Data were normalized to the averaged levels of WT samples, and quantification is shown in the right panel. Values represent mean ± SEM (n = 3; **p < 0.01; unpaired Student's t test).

(B) Depletion of m^{6}A tagging on mRNAs purified from *Mettl14* cKO NPCs. Values represent mean ± SEM (n = 3; **p < 0.01; unpaired Student's t test).

(C and D) Flow cytometry analysis of cell-cycle status of mouse NPCs. NPCs were electroporated to co-express GFP and the control shRNA or the shRNA against *Mettl3*. At day 4, NPCs were pulse labeled with EdU (10 μM) for 30 min and cultured for 9 hr, followed by EdU and DNA content (Dye-Cycle violet) staining and flow cytometry analysis. Shown are sample histograms of DNA content from GFP$^+$EdU$^+$ cells and the total cell population (C; as a reference) and quantification (D). Values in (D) represent mean ± SEM (n = 4; **p < 0.01; unpaired Student's t test).

(E–G) Embryonic mouse cortices were electroporated in utero at E13.5 to co-express GFP and shRNA-control, or GFP and shRNA-Mettl3, and analyzed at E17.5. Shown in (E) are sample confocal images. Scale bars, 50 μm. The distribution of GFP$^+$ cells in each zone (F) and the percentage of GFP$^+$Pax6$^+$ cells among total GFP$^+$ cells (G) were quantified. CP, cortical plate; IZ, intermediate zone; SVZ, subventricular zone; VZ, ventricular zone. Values represent mean ± SEM (n = 4; ***p < 0.001; **p < 0.01; unpaired Student's t test).

See also Figure S3.

from both embryonic mouse cortex in vivo and cultured cortical NPCs (Figures 3A and 3B). To further assess our model that m^{6}A methylation regulates cortical neurogenesis, we compared the phenotype of *Mettl14* cKO to knockdown of *Mettl3*, another critical component of the m^{6}A methyltransferase complex (Wang et al., 2017).

We first confirmed effective *Mettl3* knockdown (KD) with qPCR and diminished m^{6}A content in mRNAs from *Mettl3* KD cells with dot blot analysis (Figures S3A–S3C; Table S1). We next performed population cell-cycle analysis with EdU pulse-chase and flow cytometer quantification (Figure S3D). We found a significant reduction in the percentage of GFP$^+$EdU$^+$ NPCs that divided upon *Mettl3* KD (Figures 3C and 3D), similar to the effect of *Mettl14* cKO (Figures S2C and S2D).

To examine the impact of *Mettl3* KD on RGC behavior in vivo, we electroporated plasmids co-expressing GFP and the small hairpin RNA (shRNA) against mouse *Mettl3*, or the control shRNA, in utero at E13.5 and analyzed GFP$^+$ cells at E17.5. Newborn neurons normally migrate toward the cortical plate (CP) through the intermediate zone (IZ), whereas self-renewing RGCs remain in the ventricular zone (VZ) and subventricular zone (SVZ) (Taverna et al., 2014). Compared to the control group, GFP$^+$ cells with *Mettl3* KD were more abundant in the VZ and SVZ and less abundant in the CP (Figures 3E and 3F), similar to the result from EdU fate mapping in *Mettl14* cKO mice (Figure 1H). There was also a significant increase in the percentage of GFP$^+$Pax6$^+$ cells among all GFP$^+$ cells with *Mettl3* KD compared to the control group (Figure 3G).

Together, these results indicate that decreasing m^{6}A levels by either *Mettl14* cKO or *Mettl3* KD leads to consistent phenotypes of protracted cell-cycle progression of cortical NPCs and reduced differentiation of RGCs during mouse embryonic cortical neurogenesis.

m^{6}A Tags Transcripts Related to Transcription Factors, the Cell Cycle, and Neurogenesis and Promotes Their Decay

To gain insight into the molecular mechanism underlying m^{6}A regulation of cortical neurogenesis, we performed m^{6}A sequencing (m^{6}A-seq) of mouse forebrain at E13.5, a stage enriched for neural stem cells. We identified 4,055 high-confidence m^{6}A peaks corresponding to 2,059 gene transcripts (Figure S4A;

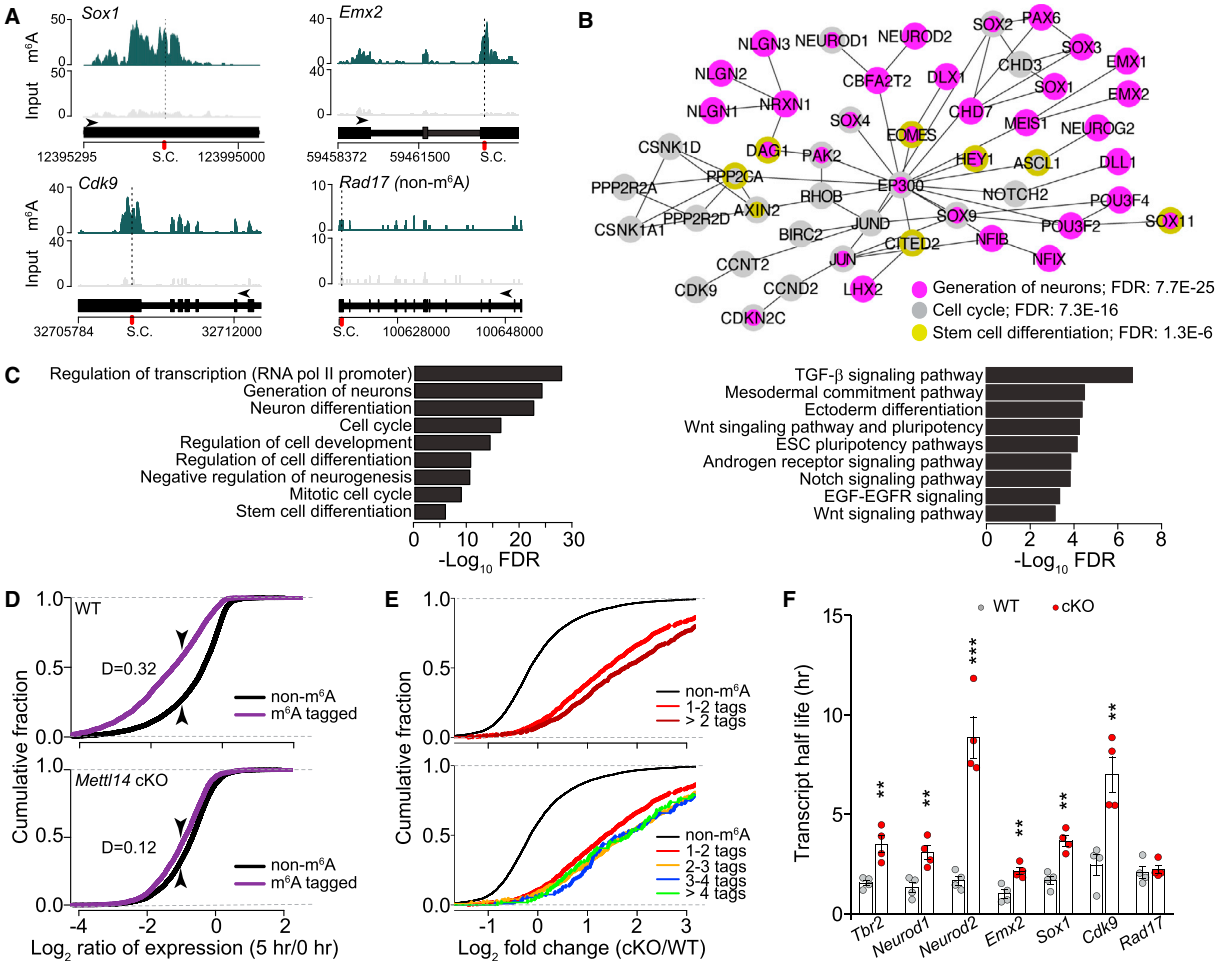

Figure 4. m^{6}A Tags Transcripts Related to Transcription Factors, the Cell Cycle, and Neuronal Differentiation in the Embryonic Mouse Brain and Promotes Their Decay

(A) Coverage plots from m^{6}A-seq of E13.5 mouse forebrains showing representative examples of m^{6}A-tagged (*Sox1*, *Emx2*, and *Cdk9*) and non-m^{6}A-tagged (*Rad17*) transcripts. Top and middle panels show read coverages normalized by library sizes from m^{6}A pull-down and input libraries, respectively, and bottom panels show gene structures (arrows point to the direction of transcription; S.C., stop codon).

(B and C) GO analysis of m^{6}A-tagged genes reveals enrichment for biological process terms related to transcription factors, neurogenesis, the cell cycle, and stem cell differentiation. Also shown is Wikipathways gene set enrichment analysis. FDR, false discovery rate.

(D) Cumulative distribution of $\log_2$(gene expression ratios) at time 5 hr after actinomycin D (ActD) treatment over time 0 hr for m^{6}A-tagged genes (purple line) and non-m^{6}A-tagged genes (black line) for WT and *Mettl14* cKO NPCs. D represents the value of Kolmogorov-Smirnov test statistic corresponding to the maximum difference between methylated and non-methylated distributions.

(E) Cumulative distribution of $\log_2$(fold change in ratios of gene expression) at 5 hr after actinomycin D treatment over time 0 hr upon *Mettl14* deletion. Top panel shows cumulative distribution for non-targets (black line) and transcripts with 1–1.9 m^{6}A sites on average (bright red line) or 2 or more sites on average (dark red line). Bottom panel shows cumulative distribution for non-targets and m^{6}A-tagged transcripts with 1–2, 2–3, 3–4, and 4 or more sites on average.

(F) Summary of half-life of a group of transcripts in WT and *Mettl14* cKO NPCs. Values represent mean ± SEM (n = 4; ***p < 0.001; **p < 0.01; unpaired Student's t test.

See also Figure S4 and Tables S2, S3, and S4.

Table S2). Similar to previous findings from cell lines (Meyer and Jaffrey, 2014), our in vivo analysis showed enriched distribution of m^{6}A sites near stop codons (Figure S4B). We found no correlation between transcript levels and m^{6}A tagging (Figure S4C). Notably, many transcripts encoding transcription factors were m^{6}A tagged, such as *Pax6*, *Sox1*, *Sox2*, *Emx2*, and *Neurog2*/*Neurogenin 2* (Figures 4A and 4B). Gene ontology (GO) and Wikipathways analyses of m^{6}A-tagged transcripts revealed enrichment of genes related to the cell cycle, stem cells, and neuronal differentiation (Figures 4A–4C; Table S3). We observed m^{6}A tagging of a similar group of transcripts in cortical NPCs derived from E13.5 mouse cortex (Figure S4D; Table S1).

To determine the functional consequence of m^{6}A tagging, we explored whether *Mettl14* deletion affects decay of m^{6}A-tagged transcripts. Cortical NPCs derived from E13.5 WT and *Mettl14* cKO mice were treated with actinomycin D to halt de novo transcription, and RNA-seq was performed 0 and 5 hr later to obtain the ratio of mRNA levels for each gene in order to measure their stability (Figure S4E). Across the transcriptomes, m^{6}A-tagged transcripts exhibited significantly lower ratios than non-m^{6}A-tagged transcripts in the WT NPCs, and this difference was reduced in cKO NPCs (Figure 4D; Table S4). Direct comparison of WT and *Mettl14* cKO NPCs showed that m^{6}A-tagged transcripts exhibited a larger increase in their ratios than non-tagged transcripts upon *Mettl14* deletion; one m^{6}A tag per transcript was sufficient to increase the ratio, and there was a minimal additional effect of more tagging sites (Figure 4E). It should be noted that our m^{6}A-seq method could not determine whether multiple sites are simultaneously methylated in the same transcript. We confirmed our result with the direct measurement of the half-life of a selected group of transcripts (Figures 4F and S4F; Table S1).

All together, these results support a model that m^{6}A methylation of mRNAs related to the cell cycle and neurogenesis confers their rapid turnover during the dynamic progress of cortical neurogenesis; a lack of m^{6}A-tagging attenuates the decay of these mRNAs, resulting in deficits in temporal specification and cell-cycle progression of NPCs.

Mettl14 Deletion Uncovers Transcriptional Prepatterning for Normal Cortical Neurogenesis

Among the 2,059 m^{6}A-tagged genes in the E13.5 mouse cortex, two major GO terms were generation of neurons and neuronal differentiation (Figure 4C). For example, the IPC markers *Tbr2* and *Neurog2* and the neuronal markers *Neurod1* and *Neurod2* (Hevner et al., 2006) were m^{6}A tagged in E13.5 forebrain in vivo (Figure 5A) and in cultured cortical NPCs (Figure S4D). qPCR analysis of total mRNA showed increased levels of *Tbr2*, *Neurog2*, *Neurod1*, and *Neurod2*, but not non-tagged *Rad17*, in *Mett14* cKO compared to WT NPCs (Figure 5B; Table S1). This result raised the possibility that neuronal lineage genes are already expressed in neural stem cells and their levels are actively suppressed post-transcriptionally by m^{6}A-dependent decay; alternatively, *Mettl14* deletion may transcriptionally upregulate these neuronal genes.

To differentiate between these two possibilities, we quantified the levels of nascent mRNA using the 4-thiouridine (4sU) metabolic labeling approach (Duffy et al., 2015). We found comparable and even lower levels of nascent mRNA of neuronal lineage genes, such as *Tbr2*, *Neurog2*, and *Neurod2*, in *Mettl14*$^{-/-}$ NPCs in comparison to WT NPCs (Figure 5B; Table S1). The lower levels of nascent mRNA observed for some neuronal lineage genes in *Mettl14* cKO NPCs could be explained by a negative feedback loop at the level of transcription, originating from elevated expression of stem cell genes, such as *Emx2* and *Sox1* (Figure 5B). Similarly, we found comparable levels of pre-mRNA for neuronal lineage genes in *Mettl14* cKO and WT NPCs (Figure S5A; Table S1), suggesting that the increase in the total mRNA of neuronal lineage genes in *Mettl14* cKO NPCs is not due to transcriptional upregulation. Together, these results support that neuronal lineage genes are already expressed in neural stem cells under normal cortical neurogenesis. Consistent with our result, mining the published single-cell RNA-seq dataset (Telley et al., 2016) revealed expression of neuronal lineage genes, such as *Tbr2*, *Neurog2*, *Neurod6*, and *Tubb3*/*Tuj1*, in individual RGCs in the embryonic mouse cortex in vivo (Figure S5B).

We next examined Tbr2 and Neurod1 protein levels in RGCs in vivo. Pax6$^+$Tbr2$^+$ cells were localized in the SVZ in WT at E17.5 but extended into the VZ in *Mettl14* cKO mice (Figures 5C and 5D). Pax6$^+$Neurod1$^+$ cells were rare but detectable just above the SVZ in WT cortices. In contrast, cKO mice exhibited a significantly increased number of Pax6$^+$Neurod1$^+$ cells with a much broader distribution, including in the SVZ and VZ (Figures 5E and 5F). To specifically examine expression in RGCs, we pulse-labeled juxtaventricular newborn cells by FlashTag (FT) (Telley et al., 2016). We found a significantly higher number of FT$^+$Pax6$^+$Tbr2$^+$ and FT$^+$Pax6$^+$Neurod1$^+$ cells in *Mettl14* cKO cortex than in WT cortex 3 hr after labeling (Figures S5C and S5D). Given that FT$^+$ cells at 3 hr upon labeling are exclusively undifferentiated RGCs (Telley et al., 2016), these results suggest that Mettl14 regulates neuronal lineage gene expression directly in RGCs.

To further assess our model that mRNA decay regulates neuronal lineage gene expression in RGCs, we performed in vivo KD experiments for the components of the CCR4-NOT complex (Cnot7 and Cnot1), a major cytoplasmic mRNA deadenylase complex responsible for mRNA decay (Du et al., 2016; Schoenberg and Maquat, 2012). Both *Cnot7* KD and *Cnot1* KD led to increased numbers of Tbr2$^+$Pax6$^+$ and Neurod1$^+$Pax6$^+$ cells and location closer to the ventricular surface compared to the control shRNA (Figures S5E and S5F), phenotypes resembling *Mettl14* cKO (Figures 5C–5F).

Taken together, our results suggest heightened transcriptional coordination and a previously unappreciated transcriptional prepatterning mechanism for mammalian cortical neurogenesis in which late IPC and neuronal genes are already transcribed in cortical neural stem cells and these transcripts are downregulated post-transcriptionally by m^{6}A-dependent decay.

METTL14 Regulates Cell-Cycle Progression of Human Cortical NPCs

We next examined whether m^{6}A function is conserved in human cortical neurogenesis. Using a previously developed protocol (Yoon et al., 2014), we differentiated human iPSCs into a highly pure population of NESTIN$^+$SOX2$^+$ NPCs (hNPCs; 96.4% ± 1% among all cells; n = 5; Figure S6A). We co-expressed GFP and the validated shRNA against human *METTL14* in these hNPCs (Figure S6B). After 4 days, we labeled cells with EdU for 30 min and performed cell cycle analysis with flow cytometer quantification 14 hr later (Figure S6C). Similar to results from mouse *Mettl14* cKO NPCs (Figures S2C and S2D), we found a significant decrease in the percentage of GFP$^+$EdU$^+$ hNPCs that divided with *METTL14* KD, indicating a delayed cell-cycle progression (Figures 6A and 6B).

We recently developed a human-iPSC-derived forebrain organoid model, which exhibits transcriptome profiles similar to fetal human cortex during development up to the second trimester

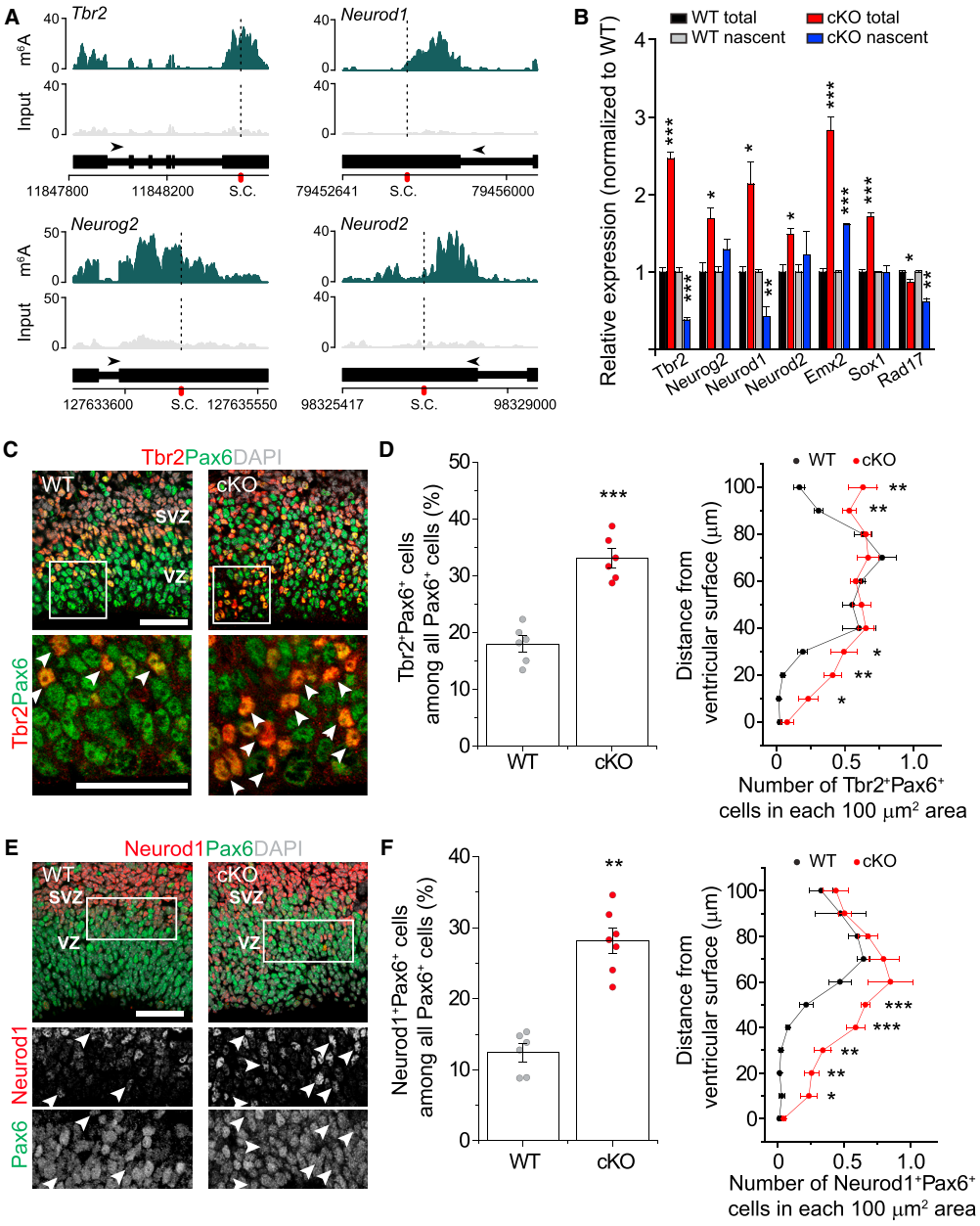

Figure 5. Post-transcriptional Regulation of Prepatterning Gene Levels and Protein Production by m^{6}A Signaling in Cortical Neural Stem Cells

(A) Coverage plots from m^{6}A-seq of E13.5 mouse forebrains showing representative examples of m^{6}A-tagged IPC (*Tbr2* and *Neurog2*) and neuronal (*Neurod1* and *Neurod2*) genes.

(B) qPCR analysis of total mRNA and 4sU-purified nascent mRNA from WT and *Mettl14* cKO NPCs. All Ct values were first normalized to *Gapdh* control (not m^{6}A-tagged), which were similar in both WT and cKO NPCs. The ratio (cKO over WT) was calculated for each experiment and values represent mean ± SEM (n = 3 cultures; ***p < 0.001; **p < 0.01; *p < 0.05; unpaired Student's t test).

(C–F) Precocious expression of Tbr2 and Neurod1 proteins in RGCs in E17.5 *Mettl14* cKO mice in vivo. Shown are sample confocal images (C and E; scale bars, 50 μm) and quantifications of the percentage of Tbr2$^+$Pax6$^+$ cells (D) or Neurod1$^+$Pax6$^+$ cells (F) among total Pax6$^+$ cells (left, n = 6) and the density distribution of Tbr2$^+$Pax6$^+$ (D) or Neurod1$^+$Pax6$^+$ cells (F) from the ventricular surface (right, n = 4). Arrows indicate Tbr2$^+$Pax6$^+$ (C) or Neurod1$^+$Pax6$^+$ cells (E). Values in (D) and (F) represent mean ± SEM (***p < 0.001; **p < 0.01; *p < 0.05; unpaired Student's t test).

See also Figure S5.

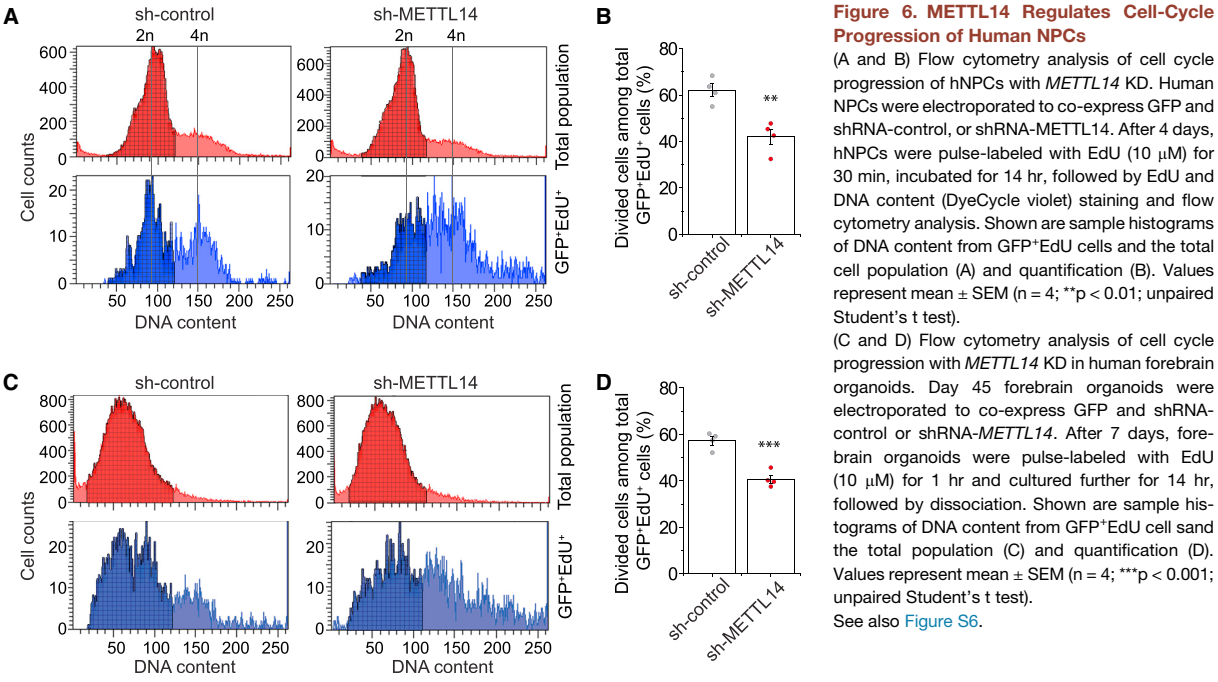

Figure 6. METTL14 Regulates Cell-Cycle Progression of Human NPCs

(A and B) Flow cytometry analysis of cell cycle progression of hNPCs with *METTL14* KD. Human NPCs were electroporated to co-express GFP and shRNA-control, or shRNA-METTL14. After 4 days, hNPCs were pulse-labeled with EdU (10 μM) for 30 min, incubated for 14 hr, followed by EdU and DNA content (DyeCycle violet) staining and flow cytometry analysis. Shown are sample histograms of DNA content from GFP$^+$EdU cells and the total cell population (A) and quantification (B). Values represent mean ± SEM (n = 4; **p < 0.01; unpaired Student's t test).

(C and D) Flow cytometry analysis of cell cycle progression with *METTL14* KD in human forebrain organoids. Day 45 forebrain organoids were electroporated to co-express GFP and shRNA-control or shRNA-*METTL14*. After 7 days, forebrain organoids were pulse-labeled with EdU (10 μM) for 1 hr and cultured further for 14 hr, followed by dissociation. Shown are sample histograms of DNA content from GFP$^+$EdU cell sand the total population (C) and quantification (D). Values represent mean ± SEM (n = 4; ***p < 0.001; unpaired Student's t test).

See also Figure S6.

(Qian et al., 2016). Around day 47, these forebrain organoids resemble mouse cortical neurogenesis at E13.5 (Figure S6D). We microinjected plasmids co-expressing GFP and the shRNA against human *METTL14*, or the control shRNA, into the lumen of forebrain organoids and performed electroporation to transfect RGCs (Figure S6E). After 7 days, we pulsed organoids with EdU for 1 hr and performed cell-cycle analysis of GFP$^+$ cells 14 hr later (Figure S6F). We observed a significant decrease in the percentage of GFP$^+$EdU$^+$ cells that divided with *METTL14* KD (Figures 6C and 6D). Together, these results indicate that m^{6}A mRNA methylation plays a conserved role in regulating cortical NPC cell cycle progression in both mouse and human.

m^{6}A-Seq of Human Forebrain Brain Organoids and Fetal Brain Reveals Conserved and Unique m^{6}A Landscape Features Compared to Embryonic Mouse Forebrain

Finally, we performed m^{6}A-seq of day 47 human forebrain organoids. We detected 11,994 high-confidence m^{6}A peaks associated with 4,702 transcripts (Figure S7A; Table S2). Our previous systematic RNA-seq analyses of human forebrain organoids at different stages revealed that transcriptomes of organoids around day 47 were similar to human fetal cortex at 8–12 post-conception weeks (PCW) (Qian et al., 2016). We further performed m^{6}A-seq of PCW11 fetal human brain and identified 10,980 high-confidence peaks associated with 5,049 transcripts (Figure S7B; Table S2). m^{6}A sites were enriched near transcription start sites and stop codons for both human samples (Figures S7C and S7D). Furthermore, m^{6}A profiles from both samples showed significant overlap (Figure 7B). GO analysis of m^{6}A-tagged transcripts shared in both samples showed enrichment of genes related to neurogenesis, neuronal differentiation, and development (Figure 7C; Table S5). Many recently identified risk genes for schizophrenia and autistic spectrum disorders have been shown to be dynamically expressed and play critical roles during mammalian embryonic brain development (Ohi et al., 2016; Tebbenkamp et al., 2014). Notably, disease ontology analysis of these m^{6}A-tagged genes shared in both human samples showed enrichment related to mental disorders, mental retardation, schizophrenia, and bipolar disorder (Figure 7C; Table S5).

We further performed comparison among m^{6}A landscapes during mouse and human cortical neurogenesis. Approximately 19.3%, 34.7%, and 31.4% of detected transcripts exhibited m^{6}A tagging in E13.5 mouse brain, day 47 human forebrain organoids, and PCW11 human fetal brain, respectively (Figure S7E). Therefore, m^{6}A mRNA methylation appears to be more prevalent in human. Among transcripts expressed in all three samples, 856 genes were commonly m^{6}A tagged (Figure 7D). These commonly m^{6}A-tagged transcripts are enriched for genes related to neurogenesis and neuronal differentiation (Figure S7F; Table S5). Notably, 1,173 transcripts were expressed in both species, but only m^{6}A-tagged in both human samples (Figure 7D). Ontology analysis of these human-specific m^{6}A-tagged transcripts showed enrichment of genes related to mental disorders and mental retardation (Figures 7E and 7F; Table S5). Among genes associated with the 108 loci recently identified for genetic risk of schizophrenia (Schizophrenia Working Group of the Psychiatric Genomics Consortium, 2014), 60 genes were m^{6}A tagged in human and 21 genes were uniquely tagged in both human forebrain organoids and fetal brain, but not in mouse E13.5 forebrain. On the other hand, the gene set of m^{6}A-tagged transcripts shared between mouse and human is enriched for oncogenic processes (Figure 7E).

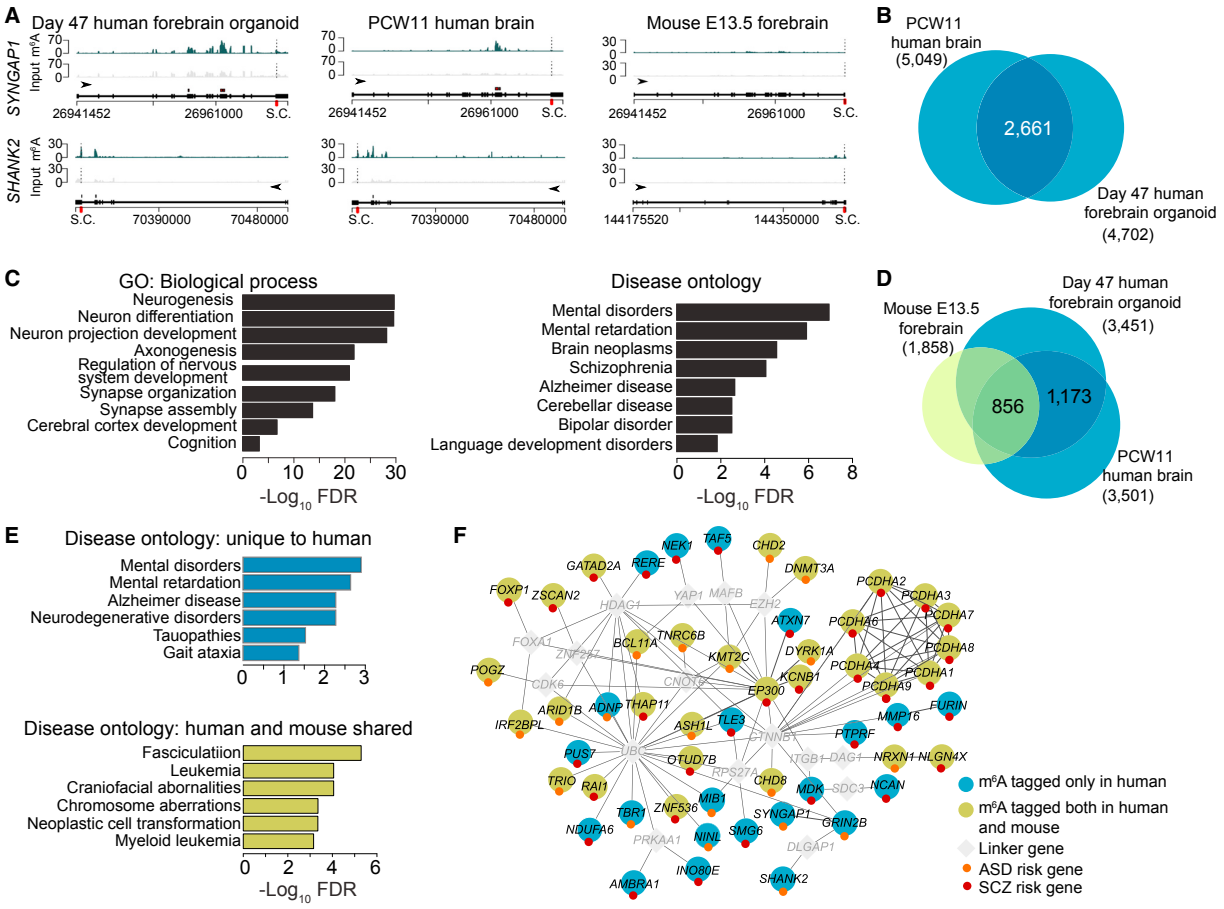

Figure 7. Conserved and Unique Features of m^{6}A mRNA Methylation in Human Forebrain Organoids, Human Fetal Brain, and Embryonic Mouse Forebrain

(A) Representative plots of two m^{6}A-tagged transcripts in day 47 human forebrain organoids and PCW11 human fetal brain, but not in mouse E13.5 forebrain.

(B) Venn diagram showing shared m^{6}A-tagged transcripts between day 47 human forebrain organoids and PCW11 fetal human brain.

(C) GO and disease ontology analyses of shared m^{6}A-tagged genes in day 47 human forebrain organoids and PCW11 human fetal brain.

(D) Venn diagram showing shared and unique m^{6}A-tagged transcripts among mouse E13.5 forebrain, day 47 human forebrain cortex, and PCW11 fetal human brain. Only ortholog genes expressed in all three samples were used for analysis.

(E and F) Disease ontology analysis of transcripts uniquely m^{6}A-tagged in human shows enrichment for neurodevelopmental diseases (E, top), including schizophrenia and autism (F), whereas disease ontology analysis of commonly m^{6}A-tagged transcripts showed enrichment for oncogenic processes (E, bottom). See also Figure S7 and Tables S2 and S5.

DISCUSSION

From flies to mammals, neurogenesis is a highly coordinated process with sequential waves of gene expression (Kohwi and Doe, 2013). Here, we revealed a critical role of m^{6}A mRNA methylation in this process in the mammalian system in vivo. Our results suggest a model in which m^{6}A tagging of transcripts related to neural stem cells, the cell cycle, and neuronal differentiation confers their rapid turnover to control the transcriptome composition at different phases of the dynamic cortical neurogenesis process. The observation of RGCs expressing markers thought to be expressed only in late IPCs and post-mitotic neurons in *Mettl14* cKO mice led to the discovery of transcriptional prepatterning in normal cortical neurogenesis and identifies m^{6}A mRNA methylation as a key mechanism to prevent precocious expression of genes of later lineage status at the protein level in stem cells. We also provide the emerging "epitranscriptomics" field with databases of m^{6}A mRNA landscapes of mouse and human cortical neurogenesis and identify intriguing human-specific features.

Transcriptional Prepatterning for Cortical Neurogenesis

The concept of prepatterning initially came from analysis of chromatin states within multipotent progenitors to regulate the fate choice for liver and pancreas (Xu et al., 2011). Recent genome-wide mapping studies have suggested that epigenetic

prepatterning is important for spatio-temporal regulation of gene expression and may be a widespread phenomenon in cell fate decision (Chen and Dent, 2014). Our study reveals transcriptional prepatterning in normal cortical neural stem cells in vivo. Consistent with our model, Pax6 has been shown to bind and activate both *Tbr2* and *Neurod1* promoters (Sansom et al., 2009). We showed that prepatterning transcripts are tagged with m^{6}A and subjected to rapid decay; therefore, most of them are present in low levels among the bulk mRNA preparation and little protein under normal conditions, a likely reason why such a mechanism has escaped detection in previous studies. While epigenetic mechanisms play a key role in transcriptional regulation during neurogenesis (Yao et al., 2016), epitranscriptomic regulation as a post-transcriptional mechanism could provide the speed and additional specificity while maintaining plasticity of gene expression. By working in concert, the epigenetic landscape can permit transcription of certain genes, such as genes defining late lineage states, while the epitranscriptome prevents aberrant protein production. Future studies are needed to investigate whether transcriptional prepatterning is a general mechanism in fate specification of other stem cells during development.

Heightened Transcriptional Coordination of Mammalian Cortical Neurogenesis by m^{6}A

Our study provides the in vivo evidence in the mammalian system to support the emerging notion that m^{6}A methylation plays a critical role in developmental fate transition. The precise and predictable developmental schedule of cortical neurogenesis requires rapid, tightly controlled changes in gene expression (Okano and Temple, 2009). Our results suggest that epitranscriptomic m^{6}A tagging, via regulation of mRNA decay, provides a key mechanism for temporal control of dynamic gene expression, which in turn regulates cell-cycle progression of cortical neural stem cells in both mouse and human.

There are three major categories of m^{6}A-tagged transcripts in the embryonic mouse brain. First, many classic transcription factors involved in neural stem cell maintenance and neurogenesis, such as *Pax6*, *Sox2*, *Emx2*, and *Tbr2*, are m^{6}A tagged and subject to rapid decay. Second, cell-cycle-related transcripts, such as *Cdk9*, *Ccnh*/*Cyclin H*, and *Cdkn1C*/*p57*, are m^{6}A tagged. Functionally, the loss of m^{6}A tagging leads to prolonged cell-cycle progression of cortical NPCs, resulting in delayed generation of different neuronal subtypes, extension of cortical neurogenesis into postnatal stages, and deficits in astrocyte generation in vivo. Third, transcripts that were generally thought to be expressed only in later IPCs and post-mitotic neurons, such as *Neurod1* and *Neurod2*, are m^{6}A tagged and expressed in neural stem cells. While expression of transcription factors is known to overlap during different stages of mammalian cortical neurogenesis (Hevner et al., 2006), our finding suggests a greater degree of transcriptional coordination than previously thought. On the other hand, expression of detectable neuronal proteins in a significant number of RGCs located in the SVZ in the absence of *Mettl14* highlights the critical role of the epitranscriptomic mechanism in preventing precocious gene expression during the normal process of mammalian cortical neurogenesis.

Conserved and Unique Features of Human m^{6}A Landscape during Cortical Neurogenesis

Our study provides databases of m^{6}A mRNA landscapes during mouse and human cortical neurogenesis. Consistent with a similar role for m^{6}A mRNA methylation in regulating cell-cycle progression of cultured human NPCs and mouse NPCs in vitro and in vivo, the shared m^{6}A-tagged transcripts in our mouse and human samples are enriched with genes related to neural stem cells, the cell cycle, and neurogenesis. Notably, many genes associated with genetic risk for mental disorders, such as schizophrenia and autistic spectrum disorders, are m^{6}A tagged in humans, but not in mice, raising the possibility that epitranscriptomic dysregulation may contribute to these human brain disorders. So far, one association study found evidence of ALKBH5 in conferring genetic risk for major depression disorder (Du et al., 2015), and two studies identified an association between FTO mutations and growth retardation and developmental delay (Boissel et al., 2009; Daoud et al., 2016).

In summary, our study identifies a critical and conserved role of an m^{6}A epitranscriptomic mechanism in the temporal control of mammalian cortical neurogenesis via promotion of mRNA decay of transcripts related to transcription factors, neural stem cells, the cell cycle, and neuronal differentiation. Future studies will address how this epitranscriptomic mechanism interacts with various epigenetic mechanisms to coordinate dynamic transcriptomes during brain development and how dysregulation of epitranscriptomic mechanisms may contribute to brain disorders.

STAR★METHODS

Detailed methods are provided in the online version of this paper and include the following:

- KEY RESOURCES TABLE
- CONTACT FOR REAGENT AND RESOURCE SHARING
- EXPERIMENTAL MODEL AND SUBJECT DETAILS
  - Animals
  - Primary mouse NPCs
  - Human iPSC cultures and fetal brain sample
- METHOD DETAILS
  - DNA constructs
  - In utero electroporation and FlashTag
  - Immunohistology and confocal imaging
  - Mouse and human NPC electroporation
  - Human forebrain organoid culture
  - Forebrain organoid electroporation and analysis
  - Analysis of cell cycle progression by EdU pulse labeling
  - Time-lapse live imaging of mouse NPCs
  - RNA purification and quantitative RT-PCR analysis
  - Western blot analysis
  - m^{6}A dot blot assay
  - m^{6}A-sequencing
  - m^{6}A mRNA immunoprecipitation and Q-PCR
  - Bioinformatic analyses of m^{6}A-seq
  - Functional annotation and disease ontology
  - RNA degradation assay
  - Half-life measurement of m^{6}A-tagged transcripts

SUPPLEMENTAL INFORMATION

Supplemental Information includes seven figures, five tables, and two movies and can be found with this article online at http://dx.doi.org/10.1016/j.cell.2017.09.003.

AUTHOR CONTRIBUTIONS

K.-J.Y. led the project and contributed to all aspects of the study. F.R.R. performed m^{6}A-seq, RNA-seq, and bioinformatics analysis. C.V. contributed to most aspects of the study and performed all live imaging analysis. F.J. contributed to human NPC and organoid analysis. M.P. and S.R. contributed to time-lapse imaging analysis of the cell cycle. D.J.-C., Y.S., N.-S.K., Y.Z., L.Z., S.K., X.W., and P.J. contributed to additional data collection and analyses. L.C.D., X.Z., and C.H. contributed *Mett1$^{f/f}$* mice. S.C. contributed to bioinformatics analyses. G.-l.M., H.S., and K.-J.Y. conceived the project. K.-J.Y., F.R.R., C.V., G.-l.M., and H.S. wrote the manuscript.

ACKNOWLEDGMENTS

We thank K.M. Christian and J. Schnoll for comments; members of the Ming and Song laboratories for discussion; L. Liu, Y. Cai, and D.G. Johnson for technical assistance; and T.M. Hyde and D.R. Weinberger for dissected fetal human brain samples. K.-J.Y. was partially supported by a Young Investigator Award from the Brain & Behavior Research Foundation and a postdoctoral fellowship from Maryland Stem Cell Research Found (MSCRF); C.V. was partially supported by an NSF pre-doctoral fellowship and NIH training grant T32GM007445. The research was supported by grants from the NIH (R37NS047344 to H.S.; U19MH106434 to H.S and G.-l.M.; P01NS097206 to H.S., G.-l.M., P.J., and C.H.; R01MH105128 and R35NS097370 to G.-l.M.; U19AI131130 to G.-l.M. and P.J.; R01NS051630 and R01MH102690 to P.J.; and RM1HG008935 to C.H., H.S., and P.J), the Simons Foundation (SFARI grant 308988 to H.S. and SFARI grant 401625 to G.-l.M.), and the Dr. Miriam and Sheldon G. Adelson Medical Research Foundation (G.-l.M.). C.H. is a Howard Hughes Medical Institute Investigator.

Received: May 23, 2017
Revised: August 9, 2017
Accepted: August 30, 2017
Published: September 28, 2017

REFERENCES

Anders, S., Pyl, P.T., and Huber, W. (2015). HTSeq–a Python framework to work with high-throughput sequencing data. Bioinformatics *31*, 166–169.

Batista, P.J., Molinie, B., Wang, J., Qu, K., Zhang, J., Li, L., Bouley, D.M., Lujan, E., Haddad, B., Daneshvar, K., et al. (2014). m(6)A RNA modification controls cell fate transition in mammalian embryonic stem cells. Cell Stem Cell *15*, 707–719.

Beauparlant, M.A., and Drouin, G. (2014). Multiple independent insertions of 5S rRNA genes in the spliced-leader gene family of trypanosome species. Curr. Genet. *60*, 17–24.

Boissel, S., Reish, O., Proulx, K., Kawagoe-Takaki, H., Sedgwick, B., Yeo, G.S., Meyre, D., Golzio, C., Molinari, F., Kadhom, N., et al. (2009). Loss-of-function mutation in the dioxygenase-encoding FTO gene causes severe growth retardation and multiple malformations. Am. J. Hum. Genet. *85*, 106–111.

Chen, T., and Dent, S.Y. (2014). Chromatin modifiers and remodellers: regulators of cellular differentiation. Nat. Rev. Genet. *15*, 93–106.

Chen, C.Y., Ezzeddine, N., and Shyu, A.B. (2008). Messenger RNA half-life measurements in mammalian cells. Methods Enzymol. *448*, 335–357.

Chen, J., Bardes, E.E., Aronow, B.J., and Jegga, A.G. (2009). ToppGene Suite for gene list enrichment analysis and candidate gene prioritization. Nucleic Acids Res. *37*, W305–W311.

Daoud, H., Zhang, D., McMurray, F., Yu, A., Luco, S.M., Vanstone, J., Jarinova, O., Carson, N., Wickens, J., Shishodia, S., et al. (2016). Identification of a pathogenic FTO mutation by next-generation sequencing in a newborn with growth retardation and developmental delay. J. Med. Genet. *53*, 200–207.

Desrosiers, R.C., Friderici, K.H., and Rottman, F.M. (1975). Characterization of Novikoff hepatoma mRNA methylation and heterogeneity in the methylated 5′ terminus. Biochemistry *14*, 4367–4374.

Dominissini, D., Moshitch-Moshkovitz, S., Schwartz, S., Salmon-Divon, M., Ungar, L., Osenberg, S., Cesarkas, K., Jacob-Hirsch, J., Amariglio, N., Kupiec, M., et al. (2012). Topology of the human and mouse m6A RNA methylomes revealed by m6A-seq. Nature *485*, 201–206.

Du, T., Rao, S., Wu, L., Ye, N., Liu, Z., Hu, H., Xiu, J., Shen, Y., and Xu, Q. (2015). An association study of the m6A genes with major depressive disorder in Chinese Han population. J. Affect. Disord. *183*, 279–286.

Du, H., Zhao, Y., He, J., Zhang, Y., Xi, H., Liu, M., Ma, J., and Wu, L. (2016). YTHDF2 destabilizes m(6)A-containing RNA through direct recruitment of the CCR4-NOT deadenylase complex. Nat. Commun. *7*, 12626.

Duffy, E.E., Rutenberg-Schoenberg, M., Stark, C.D., Kitchen, R.R., Gerstein, M.B., and Simon, M.D. (2015). Tracking distinct RNA populations using efficient and reversible covalent chemistry. Mol. Cell *59*, 858–866.

Dwyer, N.D., Chen, B., Chou, S.J., Hippenmeyer, S., Nguyen, L., and Ghashghaei, H.T. (2016). Neural stem cells to cerebral cortex: emerging mechanisms regulating progenitor behavior and productivity. J. Neurosci. *36*, 11394–11401.

Englund, C., Fink, A., Lau, C., Pham, D., Daza, R.A., Bulfone, A., Kowalczyk, T., and Hevner, R.F. (2005). Pax6, Tbr2, and Tbr1 are expressed sequentially by radial glia, intermediate progenitor cells, and postmitotic neurons in developing neocortex. J. Neurosci. *25*, 247–251.

Ge, S., Goh, E.L., Sailor, K.A., Kitabatake, Y., Ming, G.L., and Song, H. (2006). GABA regulates synaptic integration of newly generated neurons in the adult brain. Nature *439*, 589–593.

Geula, S., Moshitch-Moshkovitz, S., Dominissini, D., Mansour, A.A., Kol, N., Salmon-Divon, M., Hershkovitz, V., Peer, E., Mor, N., Manor, Y.S., et al. (2015). Stem cells. m6A mRNA methylation facilitates resolution of naïve pluripotency toward differentiation. Science *347*, 1002–1006.

Haussmann, I.U., Bodi, Z., Sanchez-Moran, E., Mongan, N.P., Archer, N., Fray, R.G., and Soller, M. (2016). m(6)A potentiates Sxl alternative pre-mRNA splicing for robust Drosophila sex determination. Nature *540*, 301–304.

Herwig, R., Hardt, C., Lienhard, M., and Kamburov, A. (2016). Analyzing and interpreting genome data at the network level with ConsensusPathDB. Nat. Protoc. *11*, 1889–1907.

Hevner, R.F., Hodge, R.D., Daza, R.A., and Englund, C. (2006). Transcription factors in glutamatergic neurogenesis: conserved programs in neocortex, cerebellum, and adult hippocampus. Neurosci. Res. *55*, 223–233.

Jamuar, S.S., and Walsh, C.A. (2015). Genomic variants and variations in malformations of cortical development. Pediatr. Clin. North Am. *62*, 571–585.

Kim, D., Pertea, G., Trapnell, C., Pimentel, H., Kelley, R., and Salzberg, S.L. (2013). TopHat2: accurate alignment of transcriptomes in the presence of insertions, deletions and gene fusions. Genome Biol. *14*, R36.

Kohwi, M., and Doe, C.Q. (2013). Temporal fate specification and neural progenitor competence during development. Nat. Rev. Neurosci. *14*, 823–838.

Langmead, B., and Salzberg, S.L. (2012). Fast gapped-read alignment with Bowtie 2. Nat. Methods *9*, 357–359.

Lence, T., Akhtar, J., Bayer, M., Schmid, K., Spindler, L., Ho, C.H., Kreim, N., Andrade-Navarro, M.A., Poeck, B., Helm, M., and Roignant, J.Y. (2016). m(6)A modulates neuronal functions and sex determination in Drosophila. Nature *540*, 242–247.

Leng, N., Dawson, J.A., Thomson, J.A., Ruotti, V., Rissman, A.I., Smits, B.M., Haag, J.D., Gould, M.N., Stewart, R.M., and Kendziorski, C. (2013). EBSeq: an empirical Bayes hierarchical model for inference in RNA-seq experiments. Bioinformatics *29*, 1035–1043.

Li, B., and Dewey, C.N. (2011). RSEM: accurate transcript quantification from RNA-seq data with or without a reference genome. BMC Bioinformatics *12*, 323.

Li, W., Sun, W., Zhang, Y., Wei, W., Ambasudhan, R., Xia, P., Talantova, M., Lin, T., Kim, J., Wang, X., et al. (2011). Rapid induction and long-term self-renewal of primitive neural precursors from human embryonic stem cells by small molecule inhibitors. Proc. Natl. Acad. Sci. USA *108*, 8299–8304.

Li, X., Xiong, X., and Yi, C. (2016). Epitranscriptome sequencing technologies: decoding RNA modifications. Nat. Methods *14*, 23–31.

Lois, C., Hong, E.J., Pease, S., Brown, E.J., and Baltimore, D. (2002). Germline transmission and tissue-specific expression of transgenes delivered by lentiviral vectors. Science *295*, 868–872.

Love, M.I., Huber, W., and Anders, S. (2014). Moderated estimation of fold change and dispersion for RNA-seq data with DESeq2. Genome Biol. *15*, 550.

Ma, D.K., Chiang, C.H., Ponnusamy, K., Ming, G.L., and Song, H. (2008). G9a and Jhdm2a regulate embryonic stem cell fusion-induced reprogramming of adult neural stem cells. Stem Cells *26*, 2131–2141.

Macosko, E.Z., Basu, A., Satija, R., Nemesh, J., Shekhar, K., Goldman, M., Tirosh, I., Bialas, A.R., Kamitaki, N., Martersteck, E.M., et al. (2015). Highly parallel genome-wide expression profiling of individual cells using nanoliter droplets. Cell *161*, 1202–1214.

Martynoga, B., Drechsel, D., and Guillemot, F. (2012). Molecular control of neurogenesis: a view from the mammalian cerebral cortex. Cold Spring Harb. Perspect. Biol. *4*, a008359.

Matsuda, T., and Cepko, C.L. (2004). Electroporation and RNA interference in the rodent retina in vivo and in vitro. Proc. Natl. Acad. Sci. USA *101*, 16–22.

Meyer, K.D., and Jaffrey, S.R. (2014). The dynamic epitranscriptome: N6-methyladenosine and gene expression control. Nat. Rev. Mol. Cell Biol. *15*, 313–326.

Miller, J.A., Ding, S.L., Sunkin, S.M., Smith, K.A., Ng, L., Szafer, A., Ebbert, A., Riley, Z.L., Royall, J.J., Aiona, K., et al. (2014). Transcriptional landscape of the prenatal human brain. Nature *508*, 199–206.

Nord, A.S., Pattabiraman, K., Visel, A., and Rubenstein, J.L. (2015). Genomic perspectives of transcriptional regulation in forebrain development. Neuron *85*, 27–47.

Ohi, K., Shimada, T., Nitta, Y., Kihara, H., Okubo, H., Uehara, T., and Kawasaki, Y. (2016). Specific gene expression patterns of 108 schizophrenia-associated loci in cortex. Schizophr. Res. *174*, 35–38.

Okano, H., and Temple, S. (2009). Cell types to order: temporal specification of CNS stem cells. Curr. Opin. Neurobiol. *19*, 112–119.

Patil, D.P., Chen, C.K., Pickering, B.F., Chow, A., Jackson, C., Guttman, M., and Jaffrey, S.R. (2016). m(6)A RNA methylation promotes XIST-mediated transcriptional repression. Nature *537*, 369–373.

Qian, X., Nguyen, H.N., Song, M.M., Hadiono, C., Ogden, S.C., Hammack, C., Yao, B., Hamersky, G.R., Jacob, F., Zhong, C., et al. (2016). Brain-region-specific organoids using mini-bioreactors for modeling ZIKV exposure. Cell *165*, 1238–1254.

Quinlan, A.R., and Hall, I.M. (2010). BEDTools: a flexible suite of utilities for comparing genomic features. Bioinformatics *26*, 841–842.

Sansom, S.N., Griffiths, D.S., Faedo, A., Kleinjan, D.J., Ruan, Y., Smith, J., van Heyningen, V., Rubenstein, J.L., and Livesey, F.J. (2009). The level of the transcription factor Pax6 is essential for controlling the balance between neural stem cell self-renewal and neurogenesis. PLoS Genet. *5*, e1000511.

Schizophrenia Working Group of the Psychiatric Genomics Consortium (2014). Biological insights from 108 schizophrenia-associated genetic loci. Nature *511*, 421–427.

Schoenberg, D.R., and Maquat, L.E. (2012). Regulation of cytoplasmic mRNA decay. Nat. Rev. Genet. *13*, 246–259.

Shannon, P., Markiel, A., Ozier, O., Baliga, N.S., Wang, J.T., Ramage, D., Amin, N., Schwikowski, B., and Ideker, T. (2003). Cytoscape: a software environment for integrated models of biomolecular interaction networks. Genome Res. *13*, 2498–2504.

Spencer, S.L., Cappell, S.D., Tsai, F.C., Overton, K.W., Wang, C.L., and Meyer, T. (2013). The proliferation-quiescence decision is controlled by a bifurcation in CDK2 activity at mitotic exit. Cell *155*, 369–383.

Taverna, E., Götz, M., and Huttner, W.B. (2014). The cell biology of neurogenesis: toward an understanding of the development and evolution of the neocortex. Annu. Rev. Cell Dev. Biol. *30*, 465–502.

Tebbenkamp, A.T., Willsey, A.J., State, M.W., and Sestan, N. (2014). The developmental transcriptome of the human brain: implications for neurodevelopmental disorders. Curr. Opin. Neurol. *27*, 149–156.

Telley, L., Govindan, S., Prados, J., Stevant, I., Nef, S., Dermitzakis, E., Dayer, A., and Jabaudon, D. (2016). Sequential transcriptional waves direct the differentiation of newborn neurons in the mouse neocortex. Science *351*, 1443–1446.

Terry, N.H., and White, R.A. (2006). Flow cytometry after bromodeoxyuridine labeling to measure S and G2+M phase durations plus doubling times in vitro and in vivo. Nat. Protoc. *1*, 859–869.

Wang, Y., Li, Y., Toth, J.I., Petroski, M.D., Zhang, Z., and Zhao, J.C. (2014a). N6-methyladenosine modification destabilizes developmental regulators in embryonic stem cells. Nat. Cell Biol. *16*, 191–198.

Wang, Z., Fan, M., Candas, D., Zhang, T.Q., Qin, L., Eldridge, A., Wachsmann-Hogiu, S., Ahmed, K.M., Chromy, B.A., Nantajit, D., et al. (2014b). Cyclin B1/Cdk1 coordinates mitochondrial respiration for cell-cycle G2/M progression. Dev. Cell *29*, 217–232.

Wang, X., Huang, J., Zou, T., and Yin, P. (2017). Human m(6)A writers: two subunits, 2 roles. RNA Biol. *14*, 300–304.

Wen, Z., Nguyen, H.N., Guo, Z., Lalli, M.A., Wang, X., Su, Y., Kim, N.S., Yoon, K.J., Shin, J., Zhang, C., et al. (2014). Synaptic dysregulation in a human iPS cell model of mental disorders. Nature *515*, 414–418.

Xu, C.R., Cole, P.A., Meyers, D.J., Kormish, J., Dent, S., and Zaret, K.S. (2011). Chromatin "prepattern" and histone modifiers in a fate choice for liver and pancreas. Science *332*, 963–966.

Xu, M., Lee, E.M., Wen, Z., Cheng, Y., Huang, W.K., Qian, X., Tcw, J., Kouznetsova, J., Ogden, S.C., Hammack, C., et al. (2016). Identification of small-molecule inhibitors of Zika virus infection and induced neural cell death via a drug repurposing screen. Nat. Med. *22*, 1101–1107.

Yao, B., Christian, K.M., He, C., Jin, P., Ming, G.L., and Song, H. (2016). Epigenetic mechanisms in neurogenesis. Nat. Rev. Neurosci. *17*, 537–549.

Yoon, K.J., Nguyen, H.N., Ursini, G., Zhang, F., Kim, N.S., Wen, Z., Makri, G., Nauen, D., Shin, J.H., Park, Y., et al. (2014). Modeling a genetic risk for schizophrenia in iPSCs and mice reveals neural stem cell deficits associated with adherens junctions and polarity. Cell Stem Cell *15*, 79–91.

Yoon, K.J., Song, G., Qian, X., Pan, J., Xu, D., Rho, H.S., Kim, N.S., Habela, C., Zheng, L., Jacob, F., et al. (2017). Zika-virus-encoded ns2a disrupts mammalian cortical neurogenesis by degrading adherens junction proteins (published online August 16, 2017). Cell Stem Cell. http://dx.doi.org/10.1016/j.stem.2017.07.014.

Zhang, B., Kirov, S., and Snoddy, J. (2005). WebGestalt: an integrated system for exploring gene sets in various biological contexts. Nucleic Acids Res. *33*, W741–W748.

Zhang, Y., Liu, T., Meyer, C.A., Eeckhoute, J., Johnson, D.S., Bernstein, B.E., Nusbaum, C., Myers, R.M., Brown, M., Li, W., and Liu, X.S. (2008). Model-based analysis of ChIP-seq (MACS). Genome Biol. *9*, R137.

Zhao, B.S., Roundtree, I.A., and He, C. (2017a). Post-transcriptional gene regulation by mRNA modifications. Nat. Rev. Mol. Cell Biol. *18*, 31–42.

Zhao, B.S., Wang, X., Beadell, A.V., Lu, Z., Shi, H., Kuuspalu, A., Ho, R.K., and He, C. (2017e). m(6)A-dependent maternal mRNA clearance facilitates zebrafish maternal-to-zygotic transition. Nature *542*, 475–478.

STAR★METHODS

KEY RESOURCES TABLE

REAGENT or RESOURCE	SOURCE	IDENTIFIER
Antibodies		
Rabbit anti-Pax6	BioLegend	PRB-278P
		RRID: AB_2313780
Mouse anti-Pax6	BD Bioscience	561664
		RRID: AB_10895587
Rabbit anti-Tbr2	Abcam	ab23345
		RRID: AB_778267
Chicken anti-GFP	Aveslab	GFP-1020
		RRID: AB_10000240
Rabbit anti-Ki67	Thermo Fisher	RM-9106
		RRID: AB_2335745
Goat anti-Sox2	Santa Cruz	sc-17320
		RRID: AB_2286684
Chicken anti-Nestin	Aveslab	NES
		RRID: AB_2314882
Rabbit anti-m^{6}A	Synaptic Systems	202 003
		RRID: AB_2279214
Mouse anti-m^{6}A	Synaptic Systems	202 111
		RRID: AB_2619891
Rabbit anti-Actin	Cytoskeleton	AAN01
		RRID: AB_10708070
Rabbit anti-GFAP	Dako	Z0334
		RRID: AB_10013382
Mouse anti-βIIITubulin (TuJ1)	Sigma-Aldrich	T3952
		RRID: AB_1841226
Rabbit anti-S100β	Abcam	ab52642
		RRID: AB_882426
Mouse anti-SATB2	Abcam	ab92446
		RRID: AB_10563678
Rabbit anti-Tbr1	Abcam	ab31940
		RRID: AB_2200219
Rat anti-CTIP2	Abcam	ab18465
		RRID: AB_2064130
Rabbit anti-Phospho-Histone H3	Cell Signaling	9701S
		RRID: AB_331534
Rabbit anti-Mettl14	ABclonal	AB8530
Mouse anti-Neurod1	Abcam	ab60704
		RRID:AB_943491
Goat anti-rabbit IgG-HRP	Santa Cruz	sc-2004
		RRID: AB_631746
Goat anti-mouse IgG-HRP	Santa Cruz	sc-2005
		RRID: AB_631736

(*Continued on next page*)

Continued

REAGENT or RESOURCE	SOURCE	IDENTIFIER
Chemicals, Peptides, and Recombinant Proteins		
Actinomycin D	Sigma-Aldrich	A1410
DAPI	Thermo Fisher Scientific	D1306
		RRID: AB_2629482
StemPro Accutase Cell Dissociation Reagent	Thermo Fisher Scientific	A1110501
Matrigel Matrix	Corning	354277
7-AAD	Thermo Fisher Scientific	A1310
Vybrant DyeCycle Violet	Thermo Fisher Scientific	V35003
Y-27632	Cellagen Technology	C9127-2 s
EdU	Thermo Fisher Scientific	A10044
Phosphatase Inhibitor Cocktail	Cell Signaling	5870
Protease Inhibitor Cocktail	Sigma	P8340
4x Laemmli Sample Buffer	Bio-Rad	1610747
Methylene blue	Sigma-Aldrich	M9140
A83-01	StemCell Technologies	72022
Dorsomorphin	StemCell Technologies	72102
SB431542	StemCell Technologies	72232
CHIR99021	StemCell Technologies	72052
Dulbecco's Phosphate-Buffered Saline (DPBS)	Corning	21-031
Dulbecco's Modification of Eagle's Medium (DMEM)	Corning	10-013
DMEM/F-12, HEPES	GIBCO	11330-032
Neurobasal Medium	GIBCO	21103049
KnockOut Serum Replacement	GIBCO	10828028
GlutaMAX Supplement	GIBCO	35050061
MEM Non-Essential Amino Acids Solution	GIBCO	11140050
Penicillin-Streptomycin (10,000 U/mL)	GIBCO	15140122
2-Mercaptoethanol	GIBCO	21985023
N-2 Supplement	GIBCO	17502048
B-27 Supplement	GIBCO	17504044
Matrigel Growth Factor Reduced (GFR) Basement Membrane Matrix	Corning	354230
Insulin solution	Sigma-Aldrich	I0516
Fetal Bovine Serum (FBS)	Corning	35-010
0.1% Gelatin in Water	StemCell Technologies	7903
Advanced DMEM/F-12	GIBCO	12634010
Human recombinant LIF	StemCell Technologies	78055
Compound E	StemCell Technologies	73952
Costar 6 Well Clear Flat Bottom Ultra Low Attachment plate	Sigma-Aldrich	CLS3471
Recombinant Human FGF-basic	Peprotech	100-18B
SUPERase In RNase Inhibitor	Thermo Fisher Scientific	AM2694
TURBO DNase (2 U/μL)	Thermo Fisher Scientific	AM2238
N6-Methyladenosine monophosphate sodium salt	Sigma-Aldrich	M2780
Agencourt AMPure XP	Beckman	A63880
Dynabeads Protein G for Immunoprecipitation	Thermo Fisher Scientific	10003D
CellTrace CFSE	Thermo Fisher Scientific	C34554
luciferase control RNA	Promega	L4561

(*Continued on next page*)

Continued

REAGENT or RESOURCE	SOURCE	IDENTIFIER
TRIzol Reagent	Thermo Fisher Scientific	15596026
4-thiouridine	Carbosynth	T4509
MTSEA biotin- XX	Biotium	90066
Dimethylformamide (DMF)	Sigma-Aldrich	D4551
Pierce Streptavidin Magnetic Bead	Thermo Fisher Scientific	88816
Critical Commercial Assays		
Click-iT EdU Assay Kits for Flow Cytometry	Thermo Fisher Scientific	C10635
Click-iT EdU Alexa Fluor 488 Imaging Kit	Thermo Fisher Scientific	C10337
Click-iT EdU Alexa Fluor 647 Imaging Kit	Thermo Fisher Scientific	C10340
Dynabeads mRNA Purification Kit	Thermo Fisher Scientific	61006
SuperScript III First-Strand Synthesis System	Thermo Fisher Scientific	18080051
Fast SYBR Green Master Mix	Thermo Fisher Scientific	4385610
NEBNext Ultra RNA Library Prep Kit for Illumina	New England Biolabs	E7530
Dynabeads mRNA DIRECT Purification Kit	Invitrogen	61011
RNeasy Mini Kit	QIAGEN	74106
Quant-IT PicoGreen dsDNA Assay Kit	Thermo Fisher Scientific	P7589
RNeasy MinElute Kit	QIAGEN	74204
Deposited Data		
Raw and analyzed data	This Paper	GSE99017
Experimental Models: Cell Lines		
B16-F10	ATCC	CRL-6475
		RRID: CVCL_0159
C12 (iPSC from normal human foreskin fibroblasts)	Wen et al., 2014	N/A
Experimental Models: Organisms/Strains		
Mouse: B6.Cg-Tg(Nes-cre)1Kln/J	Jackson Laboratory	003771 RRID: IMSR_JAX:003771
Mouse: *Mettl14*$^{floxed;floxed}$	From Dr. Chuan He	N/A
Mouse: Crl:CD1(ICR)	Charles River Laboratory	RRID: IMSR_CRL:22
Mouse: Crl:CF188	Charles River Laboratory	RRID:IMSR_CRL:23
Oligonucleotides		
shRNA control sequence for mouse and human: UUCUCCGAACGUGUCACGU	QIAGEN	SI03650318
shRNA targeting sequence: mouse *Mettl3*: GCACACUGAUGAATCUUUAGG	Wang et al., 2014a	N/A
shRNA targeting sequence: human *Mettl14*: CCUGAAAUUGGCAAUAUAGAA	Wang et al., 2014a	N/A
shRNA targeting sequence: mouse *Cnot1*: GUGGACAAUUUAACCAAGA	Du et al., 2016	N/A
shRNA targeting sequence: mouse *Cnot7*: AACAAGUCUACAUUACACCGC	Du et al., 2016	N/A
Primers for Q-PCR analysis	See Table S1	N/A
Recombinant DNA		
pUEG	Ge et al., 2006	N/A
cFUGW	Lois et al., 2002	Addgene plasmid 14883
pCAG-GFP	Matsuda and Cepko, 2004	Addgene plasmid: 11150
pPGK-H2B-mCherry-2A-DHB(aa994-1087)-GFP	From Dr. Sergi Regot (Spencer et al., 2013)	N/A
Software and Algorithms		
ImageJ	NIH	https://imagej.nih.gov/ij/
Imaris	Bitplane	http://www.bitplane.com/imaris/imaris

(*Continued on next page*)

Continued

REAGENT or RESOURCE	SOURCE	IDENTIFIER
MATLAB	MathWorks	https://www.mathworks.com/products/matlab.html
Bowtie2	Langmead and Salzberg, 2012	http://bowtie-bio.sourceforge.net/bowtie2/index.shtml
Tophat2	Kim et al., 2013	https://ccb.jhu.edu/software/tophat/index.shtml
Fastx Toolkit	http://hannonlab.cshl.edu/fastx_toolkit	http://hannonlab.cshl.edu/fastx_toolkit/download.html
MACS2	Zhang et al., 2008	https://github.com/taoliu/MACS/wiki/Install-macs2
BedTools	Quinlan and Hall, 2010	Bedtools.readthedocs.io/en/latest/content/installation.html
Metagene R Package	Beauparlant and Drouin, 2014	http://bioconductor.org/packages/release/bioc/html/metagene.html
HTSeq	Anders et al., 2015	http://www-huber.embl.de/HTSeq/doc/install.html
DESeq2	Love et al., 2014	https://bioconductor.org/packages/release/bioc/html/DESeq2.html
RSEM	Li and Dewey, 2011	https://github.com/deweylab/RSEM
EBSeq	Leng et al., 2013	https://github.com/lengning/EBSeq
Toppgene	Chen et al., 2009	https://toppgene.cchmc.org
ConsensusPathDB	Herwig et al., 2016	http://cpdb.molgen.mpg.de
Webgestalt	Zhang et al., 2005	http://www.webgestalt.org/option.php
Cytoscape	Shannon et al., 2003	http://www.cytoscape.org/download.php
Single-cell transcriptomic atlas of the developing neocortex	Telley et al., 2016	http://genebrowser.unige.ch/science2016/
Other		
SuperSignal West Dura Extended Duration Substrate	Thermo Fisher Scientific	34075
Nucleofector Kits for Mouse Neural Stem Cells	Lonza	VAPG-1004
Nucleofector 2b Device	Lonza	AAB-1001
Square wave electroporator	Nepa Gene	CUY21SC
Tweezers with platinum disk electrode	Nepa Gene	CUY650-5
Immun-Blot PVDF Membrane	Bio-Rad	1620177
Amersham Hybond-N^+ membrane	GE Healthcare	RPN119B
Stratagene Stratalinker 2400 UV Crosslinker	Agilent Genomics	53274-1
12-well Spinning Bioreactor	Qian et al., 2016	N/A

CONTACT FOR REAGENT AND RESOURCE SHARING

Further information and requests for resources and reagents should be directed to and will be fulfilled by the Lead Contact Hongjun Song (shongjun@mail.med.upenn.edu). There are no restrictions on any data or materials presented in this paper.

EXPERIMENTAL MODEL AND SUBJECT DETAILS

Animals

Exons 7, 8, and 9 of mouse *Mettl14* were targeted by inserting a single loxP site in intron 6 and an FRT-flanked neomycin resistance gene coupled with a loxP site in intron 9, with the consideration that they contain the DPWW active motif (Figure S1B). The targeting construct was electroporated into 129 mESCs, selected for neomycin resistance, screened for homologous recombination by Southern blotting, and selected mESC clones were used to generate chimeric mice by injection into C57BL/6J mouse blastocysts.

Chimeric mice were bred to wild-type C57BL/6J mice to test for germline transmission of the mutant allele, which was identified by PCR. The PCR-positive lines were crossed with a β-actin promoter-driven Flp recombinase to remove the neomycin resistance gene via FRT site recombination. The neomycin cassette-deleted mice were identified by PCR, and the resultant *Mettl14*$^{f/f}$ allele and *Nestin-Cre*$^{+/Tg}$ mice (Jackson Laboratory stock: 003771) were used to generate *Nestin-Cre*$^{+/Tg}$; *Mettl14*$^{+/f}$ mice and *Nestin-Cre*$^{+/+}$; *Mettl14*$^{f/f}$ mice. WT and cKO mice were generated by crossing *Nestin-Cre*$^{+/Tg}$; *Mettl14*$^{+/f}$ males and *Nestin-Cre*$^{+/+}$; *Mettl14*$^{f/f}$ females.

For in utero electroporation analysis, timed-pregnant CD1 mice (Charles River Laboratory) at E13.5 were used as previously described (Yoon et al., 2014). Timed pregnant mice were euthanized by cervical dislocation, and embryos were euthanized by decapitation before the dissection step. All animal procedures used in this study were performed in accordance with the protocol approved by the Institutional Animal Care and Use Committee of Johns Hopkins University School of Medicine.

Primary mouse NPCs

Mouse NPCs were isolated from *Mettl14* WT and cKO mouse embryonic cortices and cultured in Neurobasal medium (GIBCO BRL) containing 20 ng/ml FGF2, 20 ng/ml EGF, 5 mg/ml heparin, 2% B27 (v/v, GIBCO BRL), Glutamax (Invitrogen), Penicillin/Streptomycin (Invitrogen) on culture dishes precoated with Matrigel matrix (2%, Corning).

Human iPSC cultures and fetal brain sample

The human iPSC line used in the current study (C1) was fully characterized (Wen et al., 2014; Yoon et al., 2014). iPSCs were cultured in stem cell medium, consisting of DMEM:F12 (Invitrogen) supplemented with 20% Knockout Serum Replacer (GIBCO), 1X Non-essential Amino Acids (Invitrogen), 1X Penicillin/Streptomycin (Invitrogen), 1X 2-Mercaptoenthanol (Millipore), 1X Glutamax (Invitrogen), and 10 ng/ml FGF-2 (Peprotech). Culture medium was changed every day. Human iPSCs were passaged every week onto a new plate preseeded with irradiated CF1 mouse embryonic fibroblasts (Charles River Laboratory). Human iPSCs were detached from the plate by treatment of 1 mg/ml Collagenase Type IV (Invitrogen) for 1 hr. iPSC colonies were further dissociated into smaller pieces by manual pipetting. All studies were performed under approved protocols of Johns Hopkins University School of Medicine. Human iPSCs were differentiated into primitive hNPCs according to a previously published protocol (Li et al., 2011). Briefly, iPSCs were passaged onto MEF feeders, and after 3 days, induction medium containing Advanced DMEM:F12 (50%) and Neurobasal medium (50%), CHIR99201 (4 μM, Cellagentech), SB431542 (3 μM, Cellagentech), Bovine serum albumin (5 μg/ml, Sigma), hLIF (10 ng/ml, Millipore), Compound E (0.1 μM, EMD Millipore), Glutamax (Invitrogen), Pen/Strep, supplemented with N2 and B27 (Invitrogen), was added to the culture. After 6 days of differentiation, hNPCs were dissociated with Accutase (Invitrogen) and plated, with the aid of a ROCK inhibitor (Y-27632, 3 μM, Cellagentech), onto culture dishes precoated with Matrigel matrix (2%, Corning).

The PCW11 fetal human cortical tissue was used for m^{6}A-seq. All procedures used in this study were performed in accordance with the protocol approved by the Institutional Stem Cell Research Oversight Committee of Johns Hopkins University School of Medicine and Lieber Institute for Brain Development.

METHOD DETAILS

DNA constructs

For KD experiments for mouse genes, short hairpin RNA sequences (see Key Resources Table) were cloned into the retroviral vector expressing GFP under the control of the EF1α promoter and a specific shRNA under the control of human U6 promoter (pUEG) as previously described (Ge et al., 2006). For KD experiments for human *METTL14*, a short hairpin RNA sequence was cloned into the lentiviral vector expressing GFP under the control of the human ubiquitin C promoter and the specific shRNA under the control of human U6 promoter (cFUGW: Addgene plasmid 14883) as previously described (Yoon et al., 2014). The efficacy of each shRNA was confirmed in mouse B16-F10 cells (ATCC), or hNPCs derived from the C1 iPSC line.

In utero electroporation and FlashTag

In utero electroporation was performed as described previously (Yoon et al., 2014). In brief, timed-pregnant CD1 mice (Charles River Laboratory) at E13.5 or E14.5 were anesthetized and the uterine horns were exposed and approximately 1 to 2 μL of plasmid DNA, 0.5 μg/μl pCAG-GFP (Addgene plasmid: 11150) and 2.5 μg/μl cFUGW plasmid with the control shRNA, or the shRNA against mouse *Mettl3, Cnot1 and Cnot7*, was injected manually into the lateral ventricles of embryos using a calibrated micropipette. Five pulses (40 V, 50 ms in duration with a 950 ms interval) were delivered across the uterus with two 5-mm electrode paddles (CUY650-5, Nepa Gene) positioned on either side of the head by a square wave electroporator (CUY21SC, Nepa Gene). After electroporation, the uterus was placed back in the abdominal cavity and the wound was sutured. Mouse embryos were analyzed at E17.5. For FlashTag of RGCs, 1 μL of 10 μM of a carboxyfluorescein succinimidyl ester (CellTrace CFSE, ThermoFisher) was injected into the lateral ventricle of the E17.5 embryos using a calibrated micropipette. Mouse embryos were collected 3 hr later, fixed with 4% paraformaldehyde in PBS overnight at 4°C for analysis. All animal procedures were performed in accordance with the protocol approved by the Johns Hopkins Institutional Animal Care and Use Committee.

Immunohistology and confocal imaging

For EdU labeling, timed pregnant mice were injected with EdU (150 mg/kg bodyweight, Invitrogen) at defined time points before euthanasia. For immunostaining of tissue sections, brains were fixed with 4% paraformaldehyde in PBS overnight at 4°C as previously described (Yoon et al., 2014). Samples were cryoprotected in 30% sucrose in PBS, embedded in OCT compound, and sectioned coronally (20 μm-thickness) on a Leica CM3050S cryostat. Brain sections were blocked and permeabilized with the blocking solution (5% normal donkey serum, 3% Bovine serum albumin, and 0.1% Triton X-100 in PBS) for 1 hr at room temperature, followed by incubation with primary antibodies diluted in the blocking solution at 4°C overnight. After washing, secondary antibodies diluted in blocking solution were applied to the sections for 1 hr at room temperature. Nuclei were visualized by incubating for 10 min with 0.1 μg/ml 4,6-diamidino-2-phenylindole (DAPI, Thermo Fisher Scientific) in PBS. For EdU labeling, Click-iT EdU Alexa Fluor 647 Imaging Kit (Thermo Fisher Scientific) was used following the manufacturer's protocol (Qian et al., 2016). Stained sections were mounted with ProLong Gold anti-fade reagents (Thermo Fisher Scientific) and analyzed. All the antibodies used are listed in the Key Resources Table.

Mouse and human NPC electroporation

Approximately 1.0 X 10^6 mouse or human NPCs were resuspended in 100 μL Mouse Neural Stem Cell Nucleofector Solution from the Lonza Nucleofector Kit for Mouse Neural Stem Cells (Lonza, VAPG-1004). Additionally, 10 μg of the appropriate plasmid was added to the cell solution. The solution was then placed in a cuvette provided in the Nucleofector Kit and electroporated using a Lonza Nucleofector 2b device (LONZA) (Ma et al., 2008). Next, the cells were resuspended in NPC media as described above with Rock Inhibitor (Y-27632, 3 μM, Cellagentech) to reduce cell death. Cells were allowed to grow for at least 3 days before analysis.

Human forebrain organoid culture

Protocols for generation of forebrain organoids were detailed previously (Qian et al., 2016; Xu et al., 2016; Yoon et al., 2017). Briefly, human iPSCs were cultured in stem cell medium, consisting of DMEM:F12 (Invitrogen) supplemented with 20% Knockout Serum Replacer (GIBCO), 1X Non-essential Amino Acids (Invitrogen), 1X Penicillin/Streptomycin (Invitrogen), 1X 2-Mercaptoenthanol (Millipore), 1X Glutamax (Invitrogen), and 10 ng/ml FGF-2 (Peprotech) on irradiated CF1 mouse embryonic fibroblasts (Charles River). On day 1, iPSC colonies were detached by treatment of 1 mg/ml Collagenase Type IV (Invitrogen) for 1 hr and transferred to an Ultra-Low attachment 6-well plate (Corning Costar), containing 3 mL of stem cell medium (without FGF-2), plus 2 μM Dorsomorphine (Sigma) and 2 μM A83-01 (Tocris). On days 5-6, half of the medium was replaced with induction medium consisting of DMEM:F12, 1X N2 Supplement (Invitrogen), 1X Penicillin/Streptomycin, 1X Non-essential Amino Acids, 1X Glutamax, 1 μM CHIR99021 (Cellagentech), and 1 μM SB-431542 (Cellagentech). On day 7, organoids were embedded in Matrigel (Corning) and continued to grow in induction medium for 6 more days. On day 14, embedded organoids were mechanically dissociated from Matrigel and transferred to each well of a 12-well spinning bioreactor (SpinΩ) containing differentiation medium, consisting of DMEM:F12, 1X N2 and B27 Supplements (Invitrogen), 1X Penicillin/Streptomycin, 1X 2-Mercaptoenthanol, 1X Non-essential Amino Acids, 2.5 μg/ml Insulin (Sigma).

Forebrain organoid electroporation and analysis

Day 45 forebrain organoids were transferred into PBS solution in a 10 cm petri dish for electroporation. A mixture of 0.5 μL of plasmid DNA and 0.05% Fast green was injected into the lumen of neural tube structures in forebrain organoids using a calibrated micropipette (Yoon et al., 2017). About 3-4 locations on one side of each forebrain organoid were targeted by the injection. The DNA-injected side of the organoid was placed toward the positive electrode in the middle of 5 mm gap of electrode paddles (CUY650-5, Nepa Gene). Five pulses (40 V, 50 ms in duration with a 950 ms interval) were delivered by a square wave electroporator (CUY21SC, Nepa Gene). After electroporation, organoids were transferred back to the SpinΩ bioreactor for further culturing.

Analysis of cell cycle progression by EdU pulse labeling

Analyses of cell cycle progression of mouse NPCs, hNPCs, and dissociated human forebrain organoids were performed as described previously (Terry and White, 2006; Wang et al., 2014b). In brief, mouse or human NPCs were pulsed by 10 μM EdU (ThermoFisher) for 30 min and washed thoroughly with NPC media. For human forebrain organoids, 10 μM EdU directly applied to culture media and organoids were incubated in the SpinΩ bioreactor for 1 hr to ensure complete penetrance, then washed thoroughly with culture media. After defined time points, cells were dissociated by Accutase, fixed with 4% paraformaldehyde in PBS for 20 min at 4°C, stained with Click-iT EdU Alexa 647 Flow Cytometry Kits (ThermoFisher) or Click-iT EdU Alexa 488 Flow Cytometry Kits (ThermoFisher) for Flow Cytometry following manufacturer's protocol. Cells were stained with Vybrant DyeCycle Violet (ThermoFisher) or 7-AAD (ThermoFisher) for DNA content and applied to flow cytometry using BD LSR II Flow Cytometer (BD Bioscience). EdU^+ or GFP^+EdU^+ cells were gated and DNA content of those cells was analyzed compared to that of whole cell population. Percentages of divided cells among EdU^+ or GFP^+EdU^+ population (G_1 or G_0 phase determined by DNA content) during defined time intervals were quantified from four independent experiments.

Time-lapse live imaging of mouse NPCs

96-well glass bottom microplates (655892, Geiner bio-one) were coated with phenol red-free Matrigel (356237, Corning). After electroporation of mNPCs with 10 μg CDK2-sensor plasmid (pPGK-H2B-mCherry-DHB (aa994-1087)-GFP), cells were plated onto the microplates at a density of 3,000 cells per well and allowed to adhere overnight. Cells were imaged using a Nikon Eclipse Ti fluorescent microscope controlled by Metamorph microscopy automation software. Temperature (37°C), CO_2 (5%), and humidity were held constant throughout experiments. Five blank positions in a well containing Matrigel and media only were used to flat field mNPC images using custom software. ImageJ was used to merge the green and red channels. To quantify the total cell cycle length, time was measured from the first cell division to the next cell division of one or both daughters. To quantify the G_1 phase length, time was measured from one cell division to the time point of significant reduction in the ratio of green/red intensity in the nucleus of the cell. S phase entry was quantitatively defined as the time when the cytoplasmic/nuclear ratio of green/red was approximately 1, as previously described (Spencer et al., 2013). A nuclear marker, H2B-mCherry, was used in the plasmid sensor to accurately segment the cytoplasm and the nucleus. The time point from S phase entry through the second cell division was then quantified as S-G_2-M length.

RNA purification and quantitative RT-PCR analysis

For gene expression analysis, total RNA fraction was isolated from cultured NPC samples with RNeasy Mini Kit (QIAGEN), treated with DNaseI and reverse-transcribed into the first-strand cDNA with SuperScript III (Invitrogen). cDNAs were used for SYBR-green based quantitative real-time PCR to measure the expression level of target genes with the T method (ABI). All the primers used for quantitative PCR were listed in Table S1.

Western blot analysis

Forebrains from E17.5 embryos were quickly dissected out and homogenized in RIPA buffer (50 mM Tris pH 7.5, 120 mM NaCl, 1% Triton X-100, 0.5% Sodium Deoxycholate, 0.1% SDS, 5 mM EDTA, Phosphatase Inhibitor Cocktail (Cell Signaling), protease inhibitor cocktail (Sigma). Lysates were incubated for 15 min on ice and centrifuged at 15,000 g for 15 min at 4°C. Supernatant was collected and boiled for 5 min in Laemmli sample buffer (Bio-Rad), resolved by SDS-PAGE, transferred to PVDF membrane, and immunoblotted. Primary antibodies are listed in KEY RESOURCE TABLE. Quantification of bands was performed using ImageJ software.

m^{6}A dot blot assay

mRNA was harvested from homogenized forebrains at embryonic stages E15.5 and E17.5 using Dynabeads mRNA Direct Purification Kit (61011, Ambion). Four biological replicates were pooled for each sample to ensure sufficient concentration of mRNA. Dots were applied to an Amersham Hybond-N$^+$ membrane (GE Healthcare) in duplicate as 100 ng mRNA per 1 μL dot. After complete drying, the mRNA was crosslinked to the membrane using a UV Stratalinker 2400 by running the auto-crosslink program twice. The membrane was then washed in PBST three times and blocked with 5% skim milk in PBST for 2 hr. The PBST wash was repeated and the membrane was incubated with primary anti-m^{6}A antibody (212B11, Synaptic Systems) at 1:1000 dilution for 2 hr at room temperature. After 3 washes in PBST, the membrane was incubated in HRP-conjugated anti-mouse IgG secondary antibody for 2 hr at room temperature, then washed again 3 times in PBST. Finally, the membrane was visualized using SuperSignal West Dura Extended Duration Substrate (34075, Thermo Scientific). To confirm equal mRNA loading, the membrane was stained with 0.02% methylene blue in 0.3 M sodium acetate (pH 5.2) and quantified m^{6}A levels were normalized to amount of mRNA loaded. Four biological samples in technical duplicates for each time point were used.

m^{6}A-sequencing

m^{6}A profiling was performed as previously described (Dominissini et al., 2012). For m^{6}A profiling of mouse developing brain, forebrains from WT E13.5 embryos were dissected. For m^{6}A profiling of human organoids, 25 to 30 forebrain organoids at day 47 were used. For m^{6}A profiling of PCW11 fetal human brain, cortex from 2 PCW11 fetuses were dissected. The total RNA was extracted using RNeasy Mini Kit (QIAGEN). mRNA was isolated using the Dynabeads mRNA Purification Kit (Invitrogen) and mRNA was fragmented via sonication to 100-200 base pairs. m^{6}A pull-down was performed using a rabbit polyclonal anti-m^{6}A antibody (Synaptic systems), and immunoprecipitation with protein G dynabeads (ThermoFisher). m^{6}A-tagged mRNAs were competitively eluted from beads with free N^6-methyladenosine. cDNA libraries from pulled-down RNA and input RNA were prepared using the NEBNext Ultra RNA Library Prep Kit for Illumina. The experiment was performed with three technical replicates. For m^{6}A profiling of day 47 human forebrain organoids, the same procedure was followed, with the exception that the experiment was performed with two technical replicates because of the amount of samples required.

m^{6}A mRNA immunoprecipitation and Q-PCR

Total RNA from NPCs cultured from WT E13.5 mouse forebrain was extracted using RNeasy Mini Kit (QIAGEN) and mRNA was isolated using the Dynabeads mRNA Purification Kit (Invitrogen). 1% of input mRNA was reserved for reverse transcription. Full-length m^{6}A tagged transcripts were pulled-down using a rabbit polyclonal anti-m^{6}A antibody (Synaptic systems) and a mock pull-down was done with normal rabbit IgG (Cell Signaling Technologies). Immunoprecipitation was performed with protein G dynabeads (Thermo Fisher). m^{6}A-tagged mRNAs were competitively eluted from beads with free N^6-methyladenosine. Reverse

transcription of input, m^{6}A pull-down and mock pull-down mRNA was performed using the SuperScript III First-Strand Synthesis System for RT-PCR (Thermo Fisher). cDNA was used for SYBR-green based quantitative real-time PCR. Enrichment of m^{6}A tagged genes in m^{6}A pull-down over input was calculated by comparing relative concentrations using Ct values (2^{-Ct}) and dividing each concentration by the relative concentration of the input. The concentrations of the immunoprecipitated RNA were then divided by the concentration in the input RNA and multiplied by 100, to obtain the percentage of transcripts in the m^{6}A immunoprecipitation relative to the input. This value was then normalized to enrichment in the mock (IgG) pull-down, which was also calculated using relative concentrations to determine a percentage of the input. Primers used are listed in Table S1.

Bioinformatic analyses of m^{6}A-seq

cDNA libraries from input and m^{6}A pull-down were sequenced on the Illumina Nextseq platform, using a 50-cycle single-end run. Preprocessing of reads was performed using the FASTX toolkit (http://hannonlab.cshl.edu/fastx_toolkit/), namely adapters were clipped, poor quality reads were filtered out, and identical reads were collapsed. Preprocessed reads from E13.5 mouse forebrains were aligned to the mouse genome (build GRCm38/mm10), and reads from the human organoids and fetal brain to the human genome (build GRCh37/hg19), using Tophat2 (Kim et al., 2013) with default settings. m^{6}A-tagged regions were identified using the MACS2 peak calling algorithm (Zhang et al., 2008), with the input library as background. For identifying high confidence m^{6}A regions, peaks were intersected in a pairwise fashion among all replicates using the BedTools package (Quinlan and Hall, 2010). Peaks that overlap in at least 50% of their length among 2 or more samples were designated as high confidence m^{6}A regions.

For representative coverage plots of m^{6}A and input libraries, RNA-seq read alignments in bam format were transformed to bedGraph format and normalized for library size using the genomecov function from the BedTools package (Quinlan and Hall, 2010). Analysis of m^{6}A peak enrichment was performed based on 5 non-overlapping transcript segments defined as follows: Transcription start site (TSS) segment [TSS, TSS+200bp], 5′UTR [TSS+201bp, CDS start-1bp], coding region (CDS) [CDS start, CDS stop-101bp], stop codon segment [CDS stop-100bp, CDS stop+100bp], 3′ UTR [CDS stop+101bp, TTS]. Each high confidence peak was annotated to one of these regions using the BedTools package and fold enrichment was calculated from the ratio between observed peaks per region and expected number of peaks normalized by average region size. For analysis of correlation between gene expression levels and m^{6}A peak fold change, we calculated RPKMs from input RNA seq libraries, using gene counts obtained with the htseq-count function from the HTSeq python package (Anders et al., 2015) that were normalized by library size and gene length defined as the length of its longest transcript. Fold changes for m^{6}A peaks were obtained from MACS2 output.

Functional annotation and disease ontology

To assess enrichment of GO terms specific to a biological process, the ToppFunn module of the ToppGene Suite (Chen et al., 2009) was used. A hypergeometric probability mass function with Benjamini Hochberg FDR correction was used to identify significant enrichment for GO terms. Analysis of enrichment for Wikipathways terms was performed using ConsensusPathDB (Herwig et al., 2016), which calculates enrichment p values using the Wilcoxon's matched-pairs signed-rank test, and Benjamini Hochberg FDR correction.

Disease association analysis was performed using WebGestalt (Zhang et al., 2005), which uses a hypergeometric method and Benjamini Hochberg FDR correction. Protein interaction network figures were generated using Cytoscape 3.3.0 (Shannon et al., 2003), with the Reactome FI plugin.

RNA degradation assay

cDNA libraries were prepared from cultured NPCs from E13.5 WT and *Mettl14* cKO cortex, at 0 and 5 hr post Actinomycin D treatment, using the NEBNext Ultra RNA Library Prep Kit for Illumina. The experiment was performed with three replicates per condition. Sequencing was performed on the Illumina Nextseq platform, using a 100-cycle single-end run. Preprocessing of reads was performed using the FASTX toolkit. Gene expression levels were quantified using the RSEM package (Li and Dewey, 2011), which maps reads to the transcriptome using the aligner tool Bowtie2 (Langmead and Salzberg, 2012). Expected counts per gene per sample were combined into a count matrix, and this matrix was used as input for differential expression analysis using the EBSeq package (Leng et al., 2013), which uses empirical Bayesian methods to calculate the posterior probability of a gene being differentially expressed (PPDE). Posterior fold changes per gene between cKO and WT were obtained at time 0 and 5 hr after Actinomycin D treatment. Fold changes at 5 hr were normalized by fold changes at 0 hr (no Actinomycin D treatment) to specifically identify genes that degrade at a different slower rate in the cKO compared to WT, regardless of baseline changes in gene expression between two conditions. Genes with a normalized fold change higher than 2 in cKO over WT at 5 hr were considered to be differentially degraded (Table S4).

Half-life measurement of m^{6}A-tagged transcripts

Mouse NPCs were cultured in standard 6 well culture plates to approximately 80% confluence. Actinomycin D (Sigma) was added at a concentration of 5 μM. Cells were collected at three time points after addition (0, 3 hr, 5 hr) by washing once with PBS, then lysing the cells in Buffer RLT from the RNeasy Kit (QIAGEN) with 1% β-Mercaptoethanol. A cell scraper was used to remove all cells from the well plate. Each sample was normalized for cell number by quantifying DNA content using a Quant-IT PicoGreen dsDNA Assay Kit (ThermoFisher) according to manufacturer instructions. Equal amounts of cellular contents, as measured by DNA quantity, were

taken from each sample and 1 pg of luciferase control RNA (Promega) was added to each sample before RNA purification. Total RNA was then purified using an RNeasy Kit and reverse transcribed using the SuperScript II First-Strand Synthesis System (Thermo Fisher). Real-time PCR was performed on a Step One Plus cycler from Applied Biosystems with Fast SYBR Green Master Mix. Standard curves were generated by plotting CT values against the known initial concentration of luciferase control RNA, and then used to derive mRNA concentration of each target gene at each time point. The $\ln^{\text{mRNA concentrations}}$ at time point 0, 3 and 5 hr were then used to perform a linear regression as a function of time, and identify the slope of said line as the decay rate (k) (Figure S4F). Half life was calculated with the following formula: $t1/2=\ln 2/k\text{decay} = \ln 2/k_{decay}$ (Chen et al., 2008).

Metabolic labeling and purification of nascent RNA

4sU labeling of nascent RNA was performed as previously described (Duffy et al., 2015). Mouse NPCs from E13.5 WT and *Mettl14* cKO forebrain were cultured in standard 6 well culture plates to approximately 80% confluence, treated with 500 μM of 4sU (Carbosynth) for 1 hr, washed with PBS, and harvested with TRIzol reagent (ThermoFisher). Samples were extracted by chloroform twice and precipitated with isopropanol. Biotinylation of 4sU-RNA were carried out in a total volume of 250 μl, containing 70 μg total RNA, 10 mM HEPES (pH 7.5), 1 mM EDTA, and 5 μg MTSEA biotin- XX (Biotium) freshly dissolved in DMF (final concentration of DMF = 20%). Reactions were incubated at RT for 30 min in the dark, and excess biotin reagents were removed by chloroform extraction twice. Purified RNA was dissolved in 50 μL RNase-free water and denatured at 65°C for 10 min, followed by rapid cooling on ice for 5 min. Biotinylated RNA was separated from non-labeled RNA by incubating with 100 μL Streptavidin Magnetic Beads (ThermoFisher) for 20 min at RT. Beads were washed twice with high-salt wash buffer (500 μL each, 100 mM Tris- HCl pH 7.4, 10 mM EDTA, 1 M NaCl, and 0.1% Tween-20). 4sU-RNA was eluted with 100 μL freshly prepared 100 mM DTT followed by a second elution with an additional 100 μL 5 min later. RNA was recovered using the MinElute Spin columns (QIAGEN) according to the instructions of the manufacturer, and applied for Q-PCR analysis.

Comparison between human and mouse m^{6}A-seq datasets

For comparison of m^{6}A sequencing data from day 47 human forebrain organoids, PCW11 fetal human cortex, and mouse E13.5 forebrains, we restricted our analysis to expressed genes with a one-to-one ortholog between species. For determining expressed genes, we calculated RPKMs (as stated above) from input libraries, and used a threshold of RPKM > 1.

QUANTIFICATION AND STATISTICAL ANALYSIS

Data in figure panels reflect several independent experiments performed on different days. An estimate of variation within each group of data is indicated using standard error of the mean (SEM).

We performed unpaired Student's t test for assessing the significance of differences between two treatments (See each figure for details).

Analyses of mouse cortical neurogenesis in vivo

For quantitative analysis of electroporated neocortices, only GFP$^+$ cells localized within the dorso-lateral cortex were examined. 3 × 3 tiled images were obtained to cover the electroporated region of each coronal section with a 20x or 40x objective by scanning microscope (Zeiss LSM 800) and compared with equivalent sections in littermate counterparts. Quantifications were performed using Imaris software (Bitplane). Specifically, for quantification of cell fate after in utero electroporation, GFP$^+$ cells were marked, and GFP$^+$Pax6$^+$ cells were defined and counted based on the intensity of Pax6 immunofluorescence in GFP$^+$ cells measured with the same criteria among different groups using Imaris software. For the distribution of GFP$^+$ cells in each layer, the borders between different layers were defined by Pax6 immunofluorescence (VZ/SVZ) and DAPI staining (SVZ/IZ and IZ/CP). For quantification of cell fate in WT and *Mettl14* cKO mice at E17.5, P0 and P5, the regions of the primary somatosensory cortex were identified and the numbers of Pax6$^+$, Tbr2$^+$, S100β$^+$, Ctip2$^+$, Satb2$^+$ or Tbr1$^+$ cells were counted in each vertical column with 100 μm width. For distribution plots, the distances between soma of EdU$^+$Pax6$^+$, Pax6$^+$, Tbr2$^+$ or Neurod1$^+$ cells and the ventricular surface were calculated. Only EdU$^+$Pax6$^+$ cells within 200 μm distance from the ventricular surface were measured, and the histogram of cell location in every 20 μm interval from the ventricular surface was plotted as a percentage. For distribution plots of Pax6$^+$Tbr2$^+$ or Pax6$^+$Neurod1$^+$ cells, the distances between soma of cells and the ventricular surface were calculated and the numbers of cells per 100 μm^2 area in every 20 μm interval from the ventricular surface were plotted as density distribution. All quantifications were performed with 4-10 brain sections from at least 4 animals. Data are presented as the mean ± SEM and statistical significance was assessed using unpaired Student's t test.

DATA AND SOFTWARE AVAILABILITY

The access number for the data for m^{6}A-seq reported in this study is NCBI GEO: GSE99017.

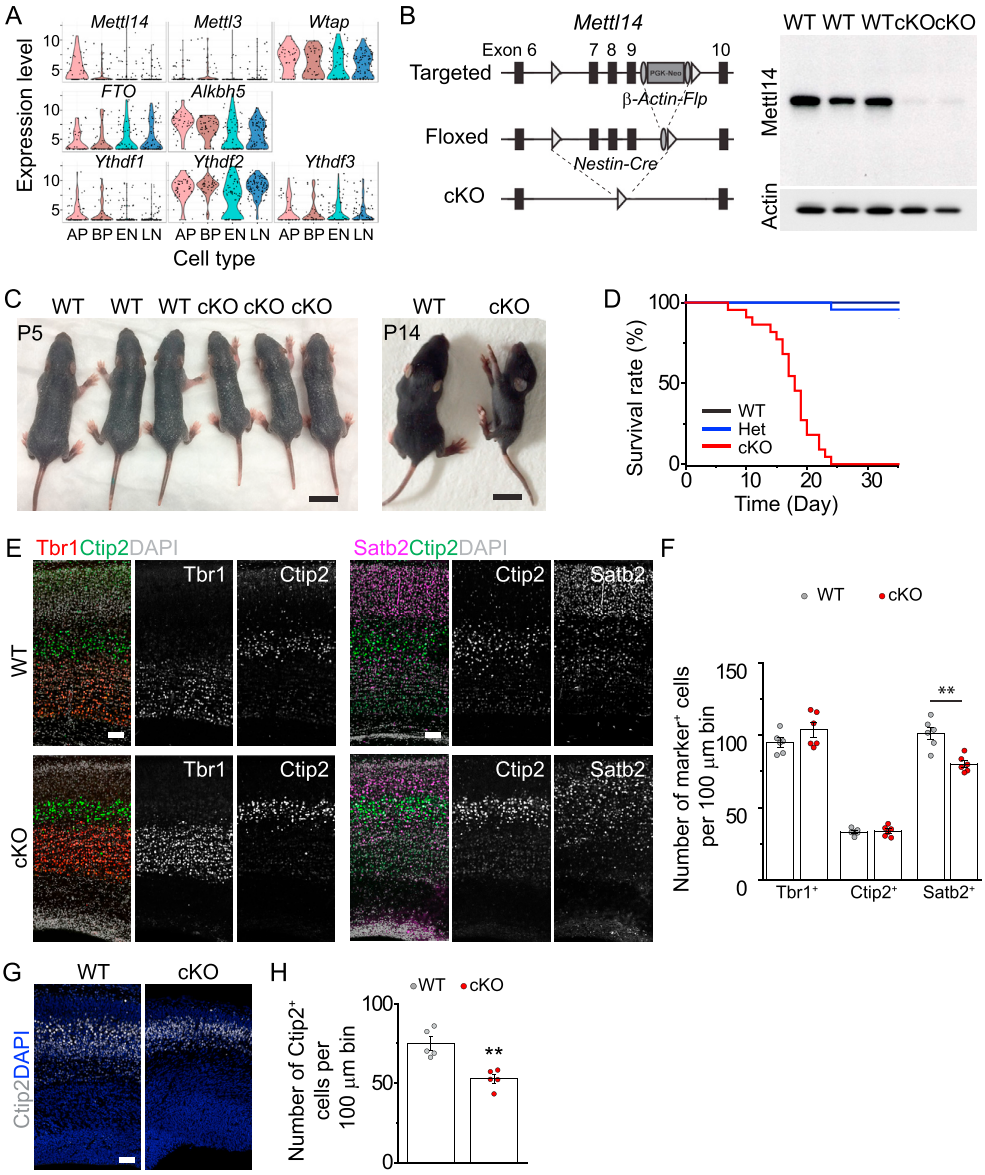

Figure S1. Nervous System *Mettl14* Deletion in Mice Results in Postnatal Lethality and Deficits in Timely Production of Cortical Neuron Subtypes, Related to Figure 1

(A) Expression of molecular mediators of m^6A signaling based on a published single-cell RNA-seq dataset of embryonic mouse cortical neurogenesis (Telley et al., 2016). Shown are the expression profiles of selected genes as violin plots, generated using the Seurat package of R (http://genebrowser.unige.ch/science2016/) (Macosko et al., 2015). AP: Apical progenitors/RGCs; BP: daughter basal progenitors/IPCs; EN: early neurons; LN: late neurons.

(B) Depletion of Mettl14 protein in the forebrain of *Nestin-Cre;Mettl14$^{f/f}$* cKO mice. Shown are the genetic deletion strategy (left) and sample western blot images from WT or cKO E17.5 forebrain lysates (right). Because *Mettl14* was only deleted in the nervous system, the minor non-neural cells contributed to the residual Mettl14 proteins (faint bands).

(C) Appearance of WT and cKO pups at P5 and P14. Note the impairment in the P14 cKO pup to maintain body balance. Scale bars, 1 cm.

(D) Survival curve of WT (n = 45), Het (n = 23) and cKO (n = 22) pups.

(E and F) Deficits in the production of upper-layer neurons in cKO cortices at P5. Shown in (E) are sample confocal images of staining for Satb2 (layer 2/3), Ctip2 (layer 5) and DAPI, or Ctip2 (layer 5), Tbr1 (layer 6) and DAPI. Scale bars, 100 μm. Quantification is shown in (E). Values represent mean ± SEM (n = 6; **: $p < 0.01$; unpaired Student's t test).

(G and H) Deficits in the production of lower-layer neurons in cKO cortices at E17.5. Shown in (E) are sample confocal images of staining for Ctip2 and DAPI. Scale bar, 100 μm. Quantification is shown in (H). Values represent mean ± SEM (n = 6; **: $p < 0.01$; unpaired Student's t test).

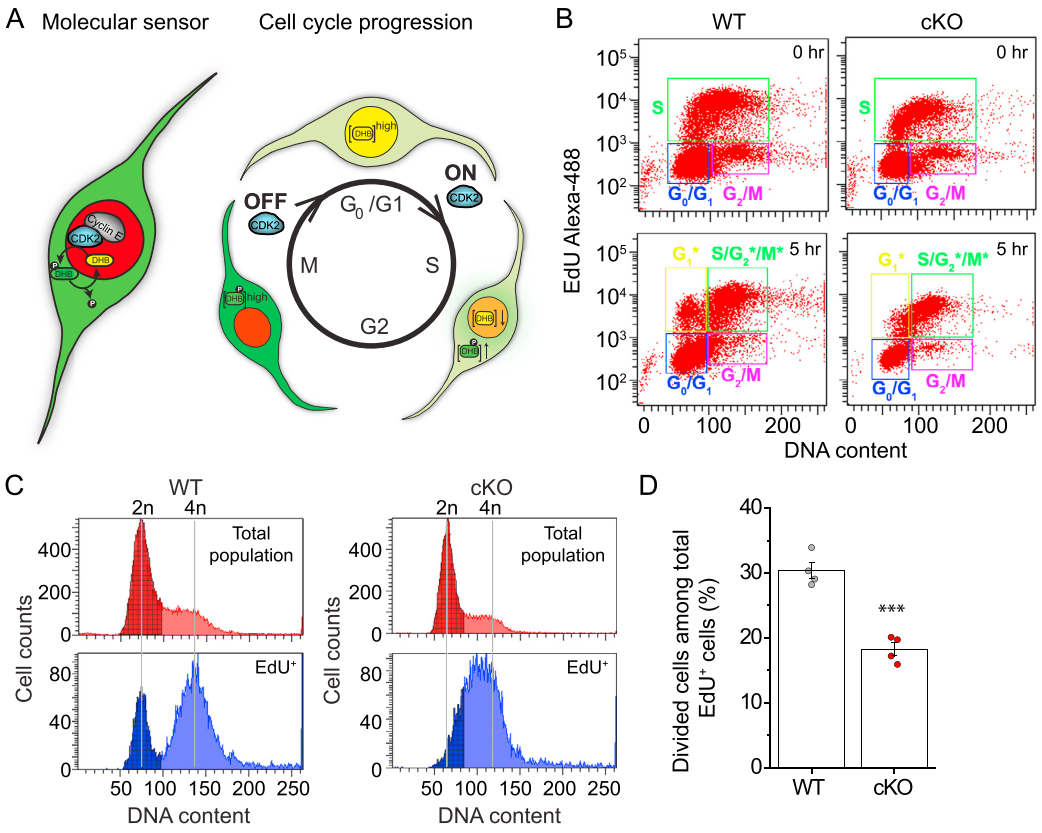

Figure S2. Flow Cytometry Analysis Reveals Delayed Cell-Cycle Progression of *Mettl14* cKO NPCs, Related to Figure 2

(A) Schematic diagrams of the dual reporter system used to track cell cycle status by time-lapse imaging. Nuclear localized H2B-mCherry and a GFP-tagged Cdk2 substrate DHB are co-expressed in the individual cell. Cdk2 becomes active during the G_1-S transition and phosphorylates DHB-GFP, which is then translocated from the nucleus to the cytoplasm. The presence of GFP in the mCherry$^+$ nucleus indicates cells in the G_1 phase, whereas translocation to the cytoplasm indicates the initiation of the S phase, and continual buildup of cytoplasmic GFP occurs until mitosis.

(B–D) Flow cytometry analysis of cell cycle progression of WT and *Mettl14* cKO NPCs. NPCs were pulse-labeled with EdU (10 μM) for 30 min, cultured for 0 or 5 hr, followed by EdU and DNA content (7AAD) staining and flow cytometry analysis. Shown in (B) are sample dot plots at 0 and 5 hr after EdU pulsing. Cells in a specific cell cycle phase were marked in a box. Note that EdU$^+$ cells (S phase at 0 hr) were segregated into divided (G_1*) and non-divided (S/G_2*/M*) populations. Shown in (C) are sample histograms of DNA content from EdU$^+$ cells and the total cell population (as a reference). Quantification is shown in (D). Values represent mean ± SEM (n = 4; ***: $p < 0.01$; unpaired Student's t test).

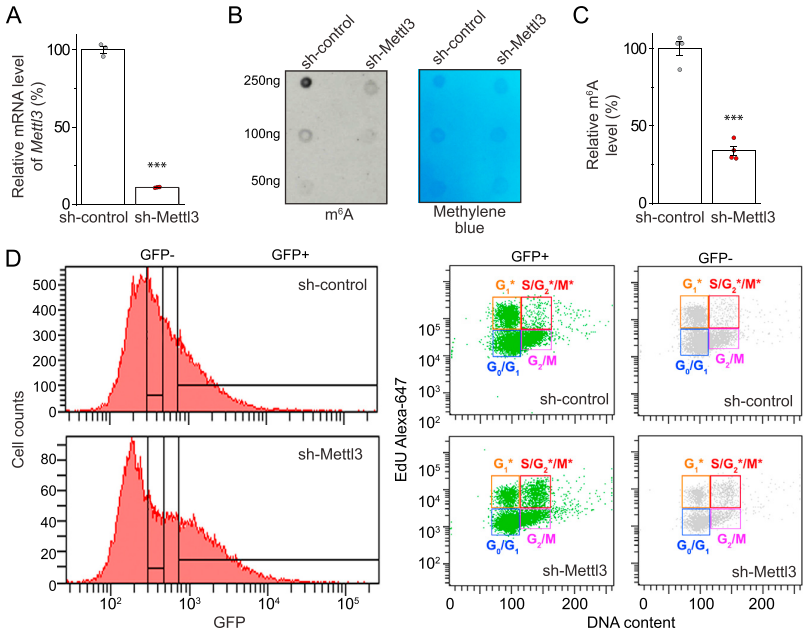

Figure S3. Mettl3 Is Essential for m^{6}A mRNA Methylation and Proper Cell-Cycle Progression of Mouse NPCs, Related to Figure 3

(A) Efficacy of the shRNA against mouse *Mettl3*. Mouse B16F10 cells were transfected with shRNA-control and shRNA-Mettl3. The amount of *Mettl3* mRNA was assessed by Q-PCR 3 days later. Values represent mean ± SEM (n = 3; ***: $p < 0.001$; unpaired Student's t test).

(B and C) Depletion of m^{6}A mRNA methylation by *Mettl3* KD. Shown are sample images of m^{6}A dot blot and methylene blue staining (as loading controls; B) and quantification (C). Data were normalized to the averaged levels of WT samples. Values represent mean ± SEM (n = 3; ***: $p < 0.01$; unpaired Student's t test).

(D) Flow cytometry analysis of cell cycle status of mouse NPCs. Mouse NPCs were electroporated to co-express GFP and shRNA-control, or shRNA-Mettl3. After 4 days, NPCs were pulse-labeled with EdU (10 μM) for 30 min, cultured for 9 hr, followed by EdU and DNA content (DyeCycle Violet) staining and flow cytometry analysis. GFP$^+$ and GFP$^-$ cells were gated separately and shown as dot plots. Note that GFP$^+$ cells with *Mettl3* KD showed accumulation of non-divided (S/G2*/M*) population.

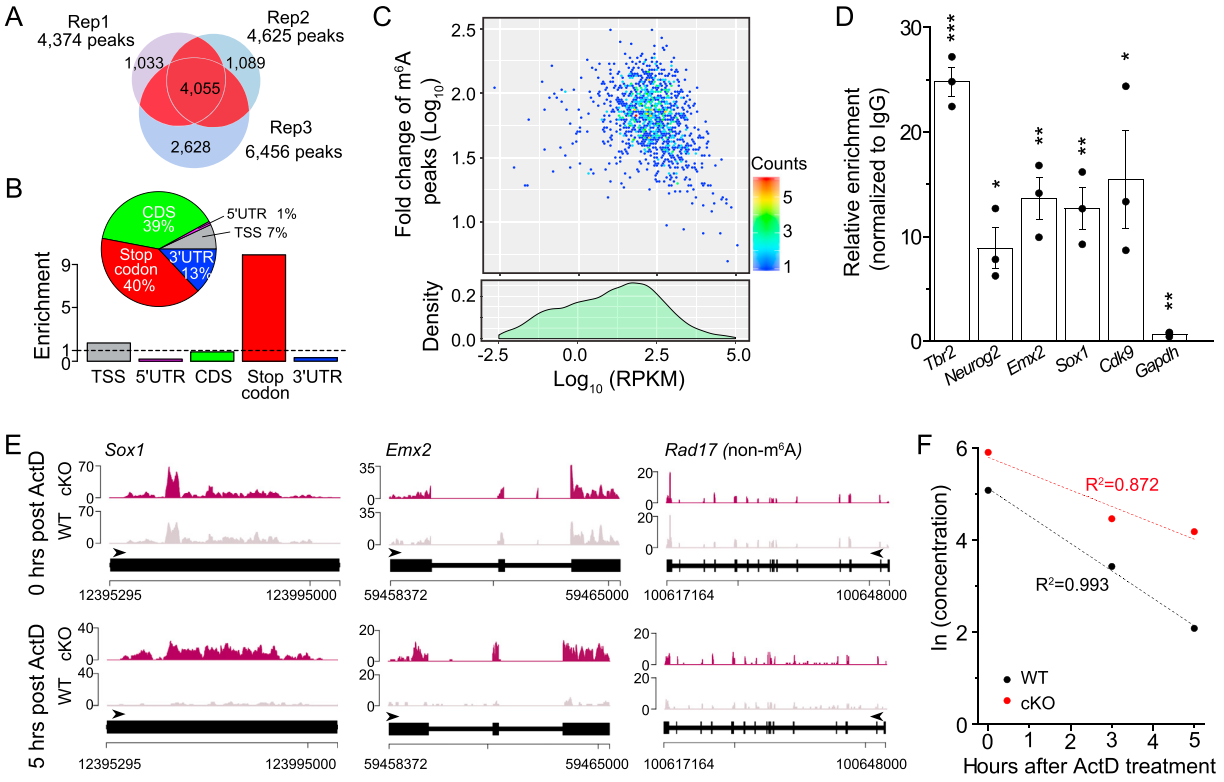

Figure S4. m^{6}A-Seq Analysis of Mouse Embryonic Forebrain, Related to Figure 4

(A) Venn diagram showing intersection among m^{6}A peaks identified in 3 independent m^{6}A-seq experiments. 4,055 high confidence peaks shared by 2 out of 3 replicates, corresponding to 2,059 genes, were used for downstream analysis.

(B) Enrichment of m^{6}A peaks in 5 non-overlapping transcript segments. Pie chart shows percentage of peaks annotated to each segment. Bar plot shows fold enrichment of peaks for each segment, normalized for the segment length.

(C) m^{6}A peaks do not correlate with transcript expression levels. Scatterplot shows gene expression levels (ln^{RPKM}) of m^{6}A-tagged genes plotted against m^{6}A peak $ln^{fold\ change}$. Histogram shows distribution of gene expression levels (ln^{RPKM}) for all transcripts detected in 3 RNA-seq input libraries.

(D) Validation of m^{6}A-tagging in specific transcripts in cortical NPCs. The enrichment of m^{6}A-tagged transcripts by IP with anti-m^{6}A antibodies over IgG was quantified by Q-PCR. Values represent mean ± SEM (n = 3; ***: $p < 0.01$; **: $p < 0.01$; *: $p < 0.05$; unpaired Student's t test).

(E) Representative coverage plots from the RNA-seq analysis at 0 or 5 hr after treatment with ActD showing increased stability of m^{6}A-tagged genes (*Sox1* and *Emx2*), but not a non m^{6}A-tagged gene (*Rad17*) in *Mettl14* cKO compared to WT NPCs.

(F) Representative plot for calculating half-life of transcripts in WT and cKO NPCs. Data for *Emx2* is plotted as an example. The ln of the transcript concentration at each time point, (0, 3, and 5 hr after Actinomycin D treatment) was plotted, and a linear regression was used to determine the slope of the resultant line. The half-life was then calculated as the ln2 divided by the absolute value of the slope of the line.

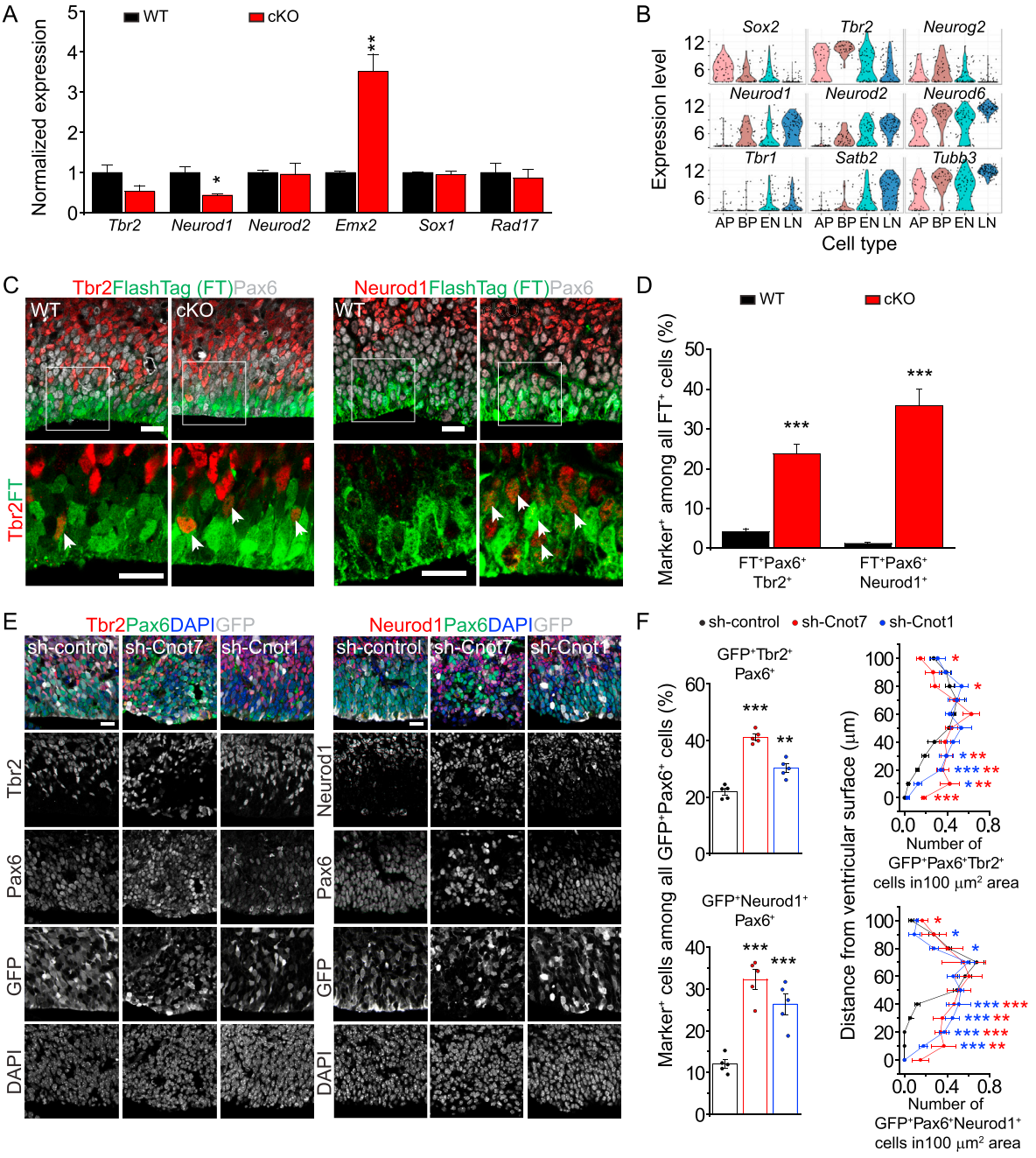

Figure S5. Expression of Neuronal Genes in RGCs of Embryonic Cortex In Vivo, Related to Figure 5

(A) Q-PCR analysis of pre-mRNA from WT and *Mettl14* cKO NPCs using pre-mRNA specific primers. All Ct values were first normalized to the *Actin* control (not m^6A-tagged), which were similar in both WT and cKO NPCs. The ratio (cKO over WT) was calculated for each experiment and values represent mean ± SEM (n = 4 cultures; **: $p < 0.01$; *: $p < 0.05$; unpaired Student's t test).

(B) Single-cell transcriptome analysis (Telley et al., 2016) reveals the expression of neuronal lineage genes in mouse embryonic cortical RGCs in vivo. Shown are the expression profiles of neural lineage genes as violin plots, similarly as in Figure S1A.

(C and D) Increased expressions of neuronal lineage genes in FlashTag$^+$ (FT$^+$) RGCs 3 hr after pulse labeling. Shown are sample confocal images (C; scale bars, 20 μm) and quantifications of the percentage of FT$^+$Tbr2$^+$Pax6$^+$ cells, or FT$^+$Neurod1$^+$Pax6$^+$ cells (D), among total FT$^+$ cells. Values represent mean ± SEM (n = 5 sections from 2 animals; ***: $p < 0.01$; unpaired Student's t test).

(legend continued on next page)

(E and F) Precocious expression of Tbr2 and Neurod1 proteins in RGCs upon KD of mRNA deadenylase components in vivo. Shown are sample confocal images (E; scale bars, 20 μm) and quantifications of the percentage of $GFP^+Tbr2^+Pax6^+$ cells, or $GFP^+Neurod1^+Pax6^+$ cells, among total GFP^+Pax6^+ cells and the density distribution of $GFP^+Tbr2^+Pax6^+$, or $GFP^+Neurod1^+Pax6^+$ cells from the ventricular surface (F). Values represent mean ± SEM (n = 5 sections from 3 animals; ***: $p < 0.001$; **: $p < 0.01$; *: $p < 0.05$; unpaired Student's t test).

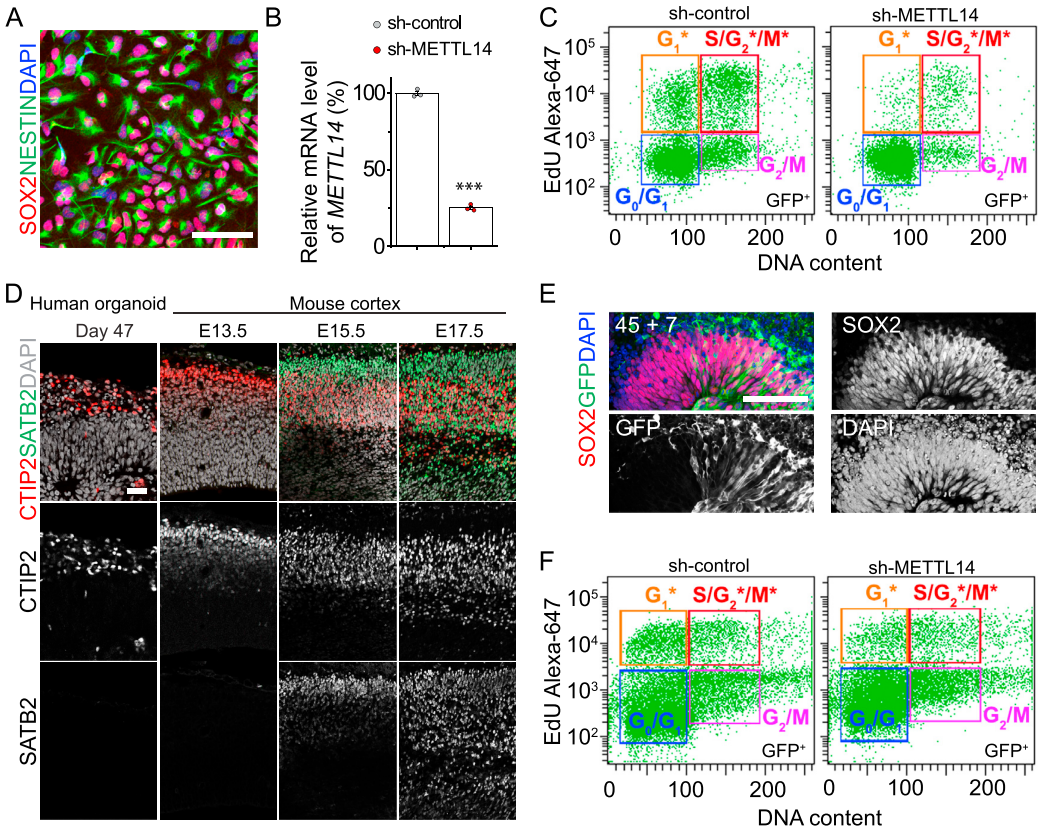

Figure S6. Mettl14 Regulates Cell-Cycle Progression of hNPCs, Related to Figure 6

(A) Validation of hNPC differentiation from human iPSCs. Shown is a sample confocal image. Scale bar, 50 μm.

(B) Efficacy of the shRNA against *METLL14.* Human NPCs were electroporated to co-express GFP and shRNA-control, or shRNA-METLL14, and dissociated 3 days later. Amount of *METLL14* mRNA in FACS-purified GFP$^+$ cells was assessed by Q-PCR. All Ct values were first normalized to the *GAPDH* control. Values represent mean ± SEM (n = 3; ***: $p < 0.01$; unpaired Student's t test).

(C) Flow cytometry analysis of cell cycle progression of hNPCs with *METTL14* KD. Similar to Figure S3D.

(D) Comparison of neuronal differentiation among day 47 human forebrain organoids and embryonic mouse cortical development at E13.5, E15.5 and E17.5. Shown are confocal images of immunostaining for CTIP2 and SATB2 and DAPI. Scale bar, 50 μm. Note that day 47 human forebrain organoids exhibit a differentiation pattern most similar to E13.5 mouse cortex.

(E) Electroporation of human forebrain organoid with shRNA-expressing plasmid. Day 45 forebrain organoids were electroporated to co-express GFP and shRNA-control, or shRNA-METTL14, by microinjection into the lumen of organoids. After 7 days, organoids were pulse-labeled with EdU (10 μM) for 30 min, and cultured further for 14 hr. Shown are sample confocal images at day 52. Scale bar, 100 μm.

(F) Flow cytometry analysis of cell cycle progression with *METTL14* KD in human forebrain organoids. Shown are sample dot plots 14 hr after EdU pulse. Cells in a specific cell cycle phase were marked within a box.

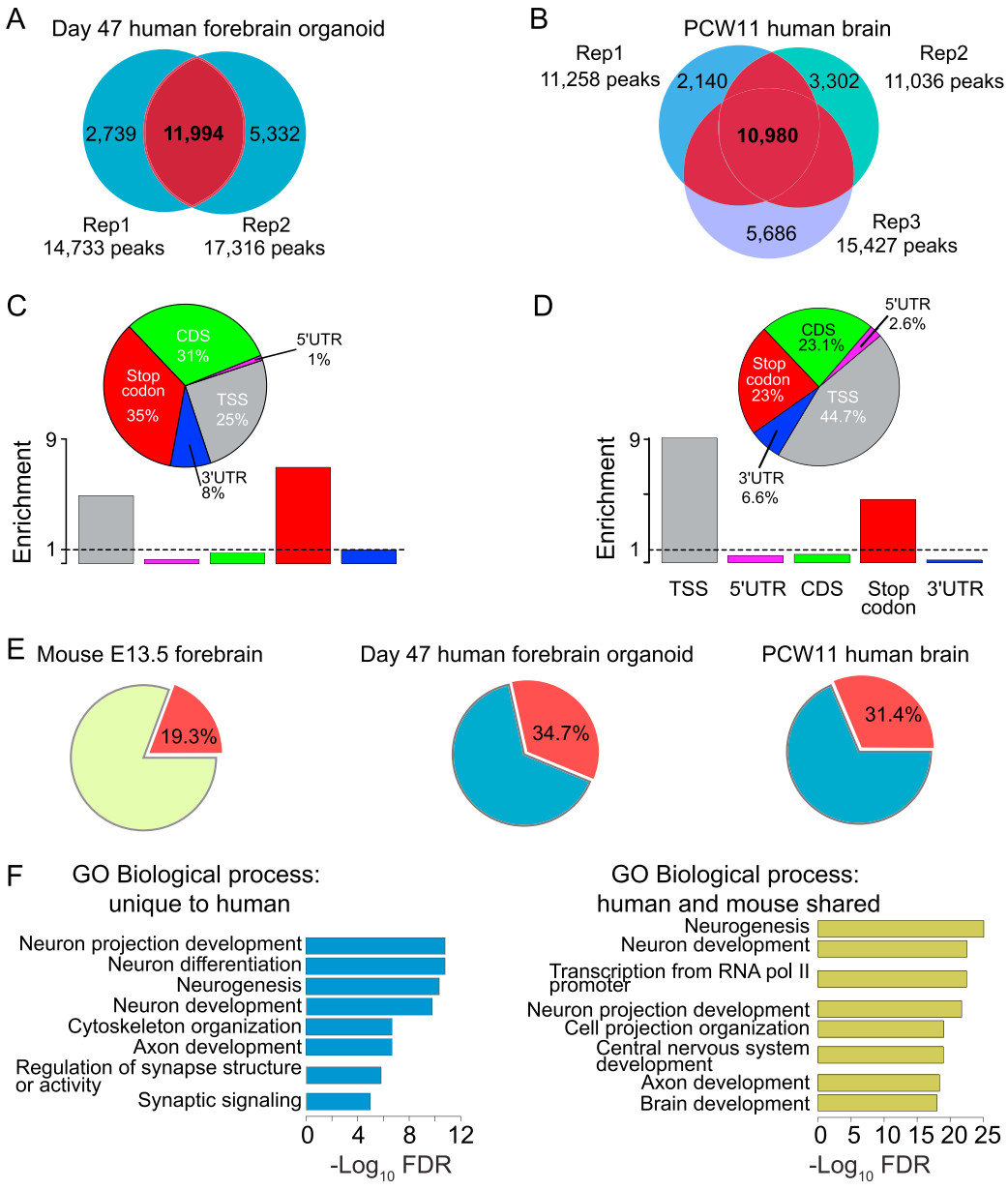

Figure S7. Comparison of m^{6}A mRNA Landscapes among Human Forebrain Organoids, Fetal Brain, and Mouse Embryonic Forebrain, Related to Figure 7

(A) Venn diagram showing intersection between m^{6}A peaks identified in 2 independent m^{6}A-seq of day 47 human forebrain organoids. 11,994 high confidence peaks corresponding to 4,702 genes were used for downstream analysis.

(B) Venn diagram showing intersection between m^{6}A peaks identified in 3 independent m^{6}A-seq of PCW11 human fetal brain. 10,980 high confidence peaks corresponding to 5,049 genes were used for downstream analysis.

(C and D) Enrichment of m^{6}A peaks in 5 non-overlapping transcript segments for day 47 human forebrain organoids (C) and PCW11 fetal human brain (D). Same as in Figure S4B.

(E) Pie charts showing the percentage of m^{6}A-tagged genes among all expressed genes in each samples.

(F) GO analysis for m^{6}A-tagged genes shared between human forebrain organoids and fetal brain, but not in mouse E13.5 forebrain (left panel), and GO analysis of m^{6}A-tagged genes shared among all three samples (right panel).